PolyPublie
Polytechnique Montréal

POLYTECHNIQUE MONTRÉAL
UNIVERSITÉ D'INGÉNIERIE

Titre: Title:	Nonlinear Aeroelastic Coupling of Aircraft Aerostructural Systems
Auteur: Author:	Miguel Gagnon
Date:	2019
Type:	Mémoire ou thèse / Dissertation or Thesis
Référence: Citation:	Gagnon, M. (2019). Nonlinear Aeroelastic Coupling of Aircraft Aerostructural Systems [Mémoire de maîtrise, Polytechnique Montréal]. PolyPublie. https://publications.polymtl.ca/3989/

Document en libre accès dans PolyPublie
Open Access document in PolyPublie

URL de PolyPublie: PolyPublie URL:	https://publications.polymtl.ca/3989/
Directeurs de recherche: Advisors:	Éric Laurendeau
Programme: Program:	Génie mécanique

Ce fichier a été téléchargé à partir de PolyPublie, le dépôt institutionnel de Polytechnique Montréal
This file has been downloaded from PolyPublie, the institutional repository of Polytechnique Montréal

https://publications.polymtl.ca

POLYTECHNIQUE MONTRÉAL
affiliée à l'Université de Montréal

Nonlinear Aeroelastic Coupling of Aircraft Aerostructural Systems

MIGUEL GAGNON
Département de génie mécanique

Mémoire présenté en vue de l'obtention du diplôme de *Maîtrise ès sciences appliquées*
Génie mécanique

Août 2019

© Miguel Gagnon, 2019.

POLYTECHNIQUE MONTRÉAL
affiliée à l'Université de Montréal

Ce mémoire intitulé :

Nonlinear Aeroelastic Coupling of Aircraft Aerostructural Systems

présenté par **Miguel GAGNON**
en vue de l'obtention du diplôme de *Maîtrise ès sciences appliquées*
a été dûment accepté par le jury d'examen constitué de :

Aouni LAKIS, président
Éric LAURENDEAU, membre et directeur de recherche
Gabriel SAIZ, membre

ACKNOWLEDGMENTS

The research work described in this thesis is funded by a "NSERC Canada Graduate Scholarships - Master's Program" and a "FRQNT Master's scholarship". The contribution of Mitacs through a "Globalink" award was also decisive in the realization of the project by funding an internship at the Institut supérieur de l'aéronautique et de l'espace (ISAE-SUPAÉRO).

RÉSUMÉ

Ce mémoire traite de l'aéroélasticité statique nonlinéaire appliquée aux avions en vol subsonique et transsonique lors de la conception préliminaire. L'objectif de ces travaux est de développer des méthodes d'analyse précises et à faible coût de calcul permettant l'exploration de l'enveloppe de design ou l'optimisation dans un contexte industriel de conception d'avions.

Le modèle d'analyses par éléments finis est basé sur les éléments de poutre Euler-Bernoulli avec résolution nonlinéaire afin de prédire les grandes déformations d'ailes très flexibles. Le modèle aérodynamique est ensuite présenté, consistant en une méthode *Vortex Lattice* avec corrections nonlinéaires visqueuses basée sur la méthode alpha modifiée et une base de données de coefficients aérodynamiques 2.5D Reynolds-Averaged Navier-Stokes. Le couplage aéroélastique est réalisé de manière itérative, en maintenant la séparation des solveurs et en utilisant une interpolation conservative des efforts aérodynamiques basée sur les fonctions de formes des éléments de poutre. Une intégration directe de la géométrie à l'étude est réalisée grâce à l'utilisation d'un modeleur 3D afin d'automatiser la génération de maillages dans les outils d'analyse.

S'ensuit la vérification du solveur structurel dans des cas linéaire et nonlinéaire en comparaison avec la théorie et NASTRAN, un solveur d'éléments finis très répandu. La robustesse de la méthode de résolution pour différentes orientations spatiales des poutres est montrée de même que l'ordre de précision de la solution. L'influence de différents paramètres comme le raffinement du maillage et l'utilisation de données visqueuses est déterminée pour un cas d'aile à allongement élevé. Les déflections et la torsion de l'aile sont comparées à des études utilisant des approches similaires et la précision des résultats numériques est discutée.

Ensuite, l'utilisation de la méthode pour des conditions de vol subsonique et transsonique est étudiée pour un cas de renversement de contrôle sur une aile rectangulaire. La présente méthode est comparée avec un autre modèle aérodynamique de fidélité moyenne quant à sa capacité à prédire l'efficacité des commandes ainsi que le comportement du système aéroélastique. Finalement, l'application des méthodes d'analyse pour l'aéroélasticité d'avions commerciaux est démontrée dans le cas du NASA CRM, pour lequel des résultats aéroélastiques numériques et expérimentaux sont disponibles.

Pour conclure, les limitations et possibles améliorations des méthodes sont discutées.

ABSTRACT

This thesis treats the subject of nonlinear static aeroelasticity applied to subsonic and transonic aircrafts in preliminary design. The objective of the work is to develop analysis methods that are accurate but with a low computational cost to allow design space exploration and optimization in an industrial commercial aircraft design process.

The finite element analysis model is based on Euler-Bernoulli beam elements with nonlinear resolution to predict the large deformation of very flexible wings. A presentation of the aerodynamic model used is then provided, comprising a classic vortex lattice method that has been modified with nonlinear viscous correction based on the modified alpha method and a database of 2.5D Reynolds-Averaged Navier-Stokes aerodynamic coefficients. The aeroelastic coupling is performed iteratively and in a segregated fashion by using a conservative interpolation of loads based on the beam element's shape functions. A direct integration of the studied geometry into the framework is also done by the use of a solid modeler to provide a basis for automatic mesh generation from the CAD model into the analysis suite.

Then, the verification of the structural solver is performed in linear and nonlinear cases against the theory and NASTRAN, a commonly used finite element solver. The robustness of the resolution method for various spatial orientation of the beams is also shown as well as the order of accuracy of the solution. The influence of different parameters such as mesh refinement and the use of viscous sectional data is then assessed for a case of subsonic high aspect-ratio wing. Wing deflection and twist are compared with other studies using similar approaches and the accuracy of the numerical results are discussed.

Then, the use of the methodology for transonic and supersonic flight conditions is studied on a case of aileron reversal for a rectangular wing. The present method is compared with another medium fidelity aerodynamic model for its ability to predict control surface effectiveness as well as the behavior of the aeroelastic system. Finally, the application of the methods to analysis of aeroelasticity of commercial aircrafts is demonstrated on the NASA CRM, for which static aeroelastic data is available both numerically from various high-fidelity studies as well as experimental tests.

To conclude, limitations and possible improvements of the methods are discussed.

TABLE OF CONTENTS

LIST OF TABLES

LIST OF FIGURES

LIST OF ACRONYMS AND ABREVIATIONS

AIAA	American Institute of Aeronautics and Astronautics
API	Application Programming Interface
CAD	Computer-aided Design
CFD	Computational Fluid Dynamics
CRM	Common Research Model
CSD	Computational Structural Dynamics
CFL	Courant-Friedrichs-Lewy number
DLM	Doublet-Lattice Method
DNS	Direct Numerical Simulation
DTS	Dual Time Stepping
EGDAS	Electronic Geometry Aircraft Design System
ETW	European Transonic Windtunnel
FEM	Finite Element Method
FFT	Fast Fourrier Transform
FSI	Fluid Structure Interaction
GCL	Geometric Conservative Law
IRS	Implicit Residual Smoothing
LCO	Limit Cycle Oscillation
LES	Large Eddy Simulation
MATD	Matrix Artificial Dissipation
NASA	National Aeronautics and Space Administration
NLFD	Nonlinear Frequency Domain
NS	Navier-Stokes
OEM	Original equipment Manufacturer
RANS	Reynolds Averaged Navier-Stokes
RHS	Right hand side
TSD	Transonic Small Disturbance
URANS	Unsteady Reynolds Averaged Navier-Stokes
VLM	Vortex-Lattice Method

α	angle-of-attack
U, U_∞	Velocity, freestream velocity vector

LIST OF APPENDICES

CHAPTER 1 INTRODUCTION

This chapter introduces the subject of aeroelasticity, and related problematics encountered in the aerospace industry. The objectives of this research project are presented as well as the outline of the thesis.

1.1 Context

In the aerospace industry, the products designed and manufactured are immensely complex and require the inputs of many fields of study as well as the coordinated efforts of dozens, if not hundreds of engineers. For example, a civil aircraft comprises millions of parts that are arranged in hundreds of systems and sub-systems each accomplishing a specific task [8]. Furthermore, with the physical limitations imposed by heavier-than-air flight and the multitude of commercial and safety constraints, there is a tremendous amount of time and resources spent in designing and optimizing each system, sub-system, and part to reduce costs and improve performance and reliability.

As such, a commercial airplane is best conceived as a "system of systems". The task of making every system can be separated with a set of defined interfaces and design requirements. The design of this product follows a sequential series of phases, mainly: conceptual, preliminary, and detailed design phases. At the beginning, each system's specifications and performance are estimated based on low fidelity methods and experience. This allows the engineers to tackle a great deal of complexity and uncertainty quickly, enabling the exploration of the design space. As the product maturity increases and several milestones are reached, the amount of personnel involved, the development costs and the amount of details also increase. The special case of Bombardier Aerospace is illustrated in Figure 1.1, where an overview of the different phases is shown as well as the corresponding decisions and milestones reached. All aerospace OEMs follow a similar philosophy according to Weiss & Amir [8].

To reflect the change in maturity, the design team also goes through changes in ownership based on the specific focus of the phase and major design challenges to be addressed. Usually, the expertise required to fulfill the requirements for the phase goes from general, high-level, and empirical knowledge, then, to aerodynamics and external shape definition, and finally individual systems and structural design and manufacturing. This has the effect that the knowledge and analysis tools mobilized are often tailored to the task at hand or adapted to solve a specific type of problem.

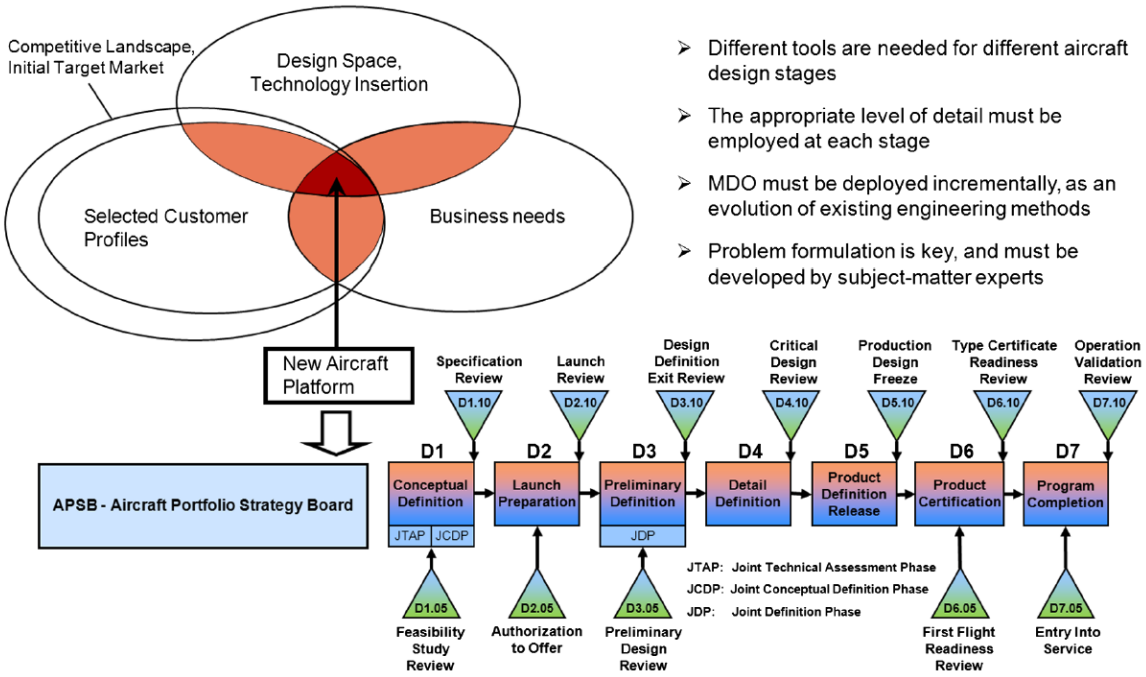

Figure 1.1 Bombardier Aerospace Engineering System (BES) showing the different design phases [1]

This design methodology also has the characteristic that decisions made in the conceptual design phase greatly impact the entirety of the schedule as shown in Figure 1.2 and are responsible for nearly 80% of the life cycle cost [2]. It is therefore crucial to develop more accurate and higher fidelity multiphysics analysis tools that have the potential to reduce the costs of design but also shorten the timeline and reduce the risks of mistakes that require a costly design change later in the program.

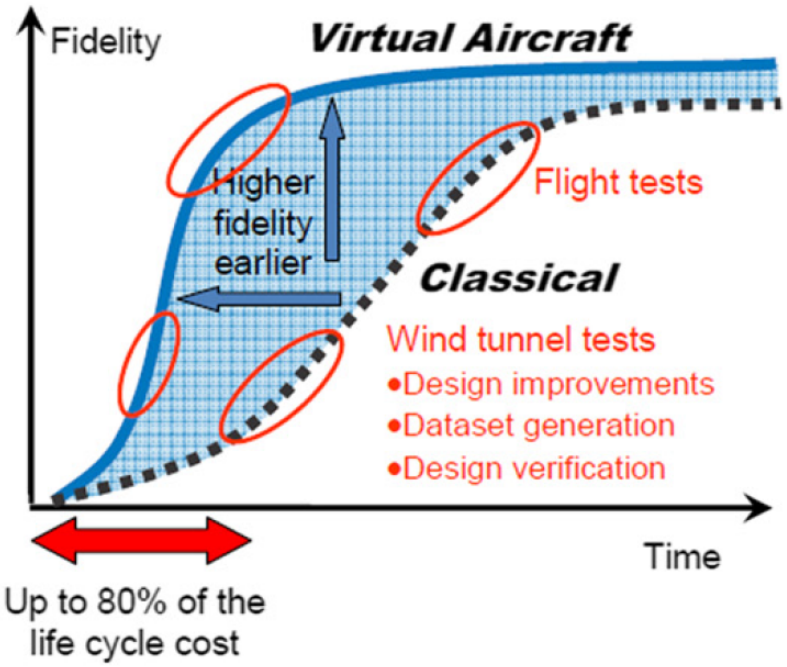

Figure 1.2 Comparison between the costs associated with a classical design methodology and a virtual aircraft approach [2]

1.2 Basic Concepts

Different phenomena arise from the interaction of aerodynamics, structural, and inertial forces and the multidisciplinary study of these phenomena is called aeroelasticity, as illustrated in Figure 1.3.

Specific technical fields can be derived from aeroelasticity:

- Flight mechanics emerges from the combination of aerodynamic and inertial forces.
- Structural vibrations are at the intersection of inertial and elastic forces.
- Static aeroelasticity relates to problems where only aerodynamic and elastic forces are considered.

In the case of aircraft design, the deformation and vibration of aircraft wings is an aeroelastic problem that greatly influences the design of the wings' structure, but also the performance in flight, the boundaries of certified operations, and the control systems.

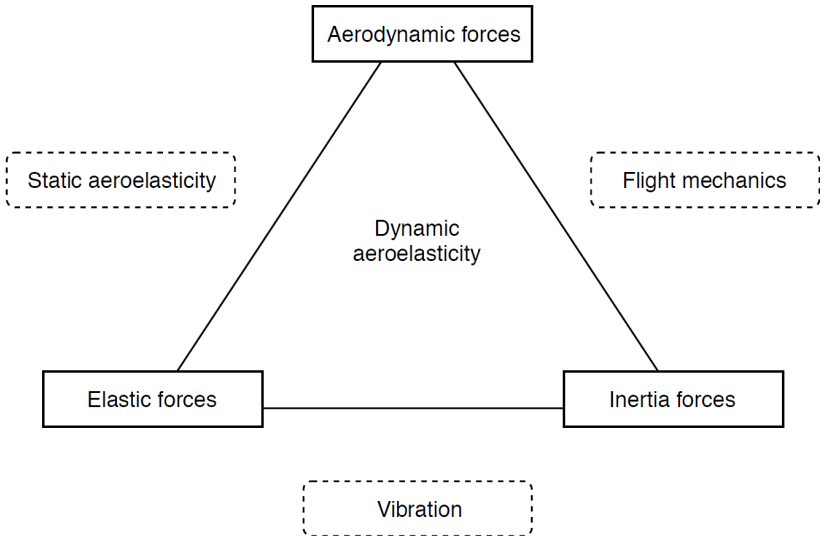

Figure 1.3 Collar's triangle showing aeroelasticity as a triangle of disciplines [3]

1.2.1 Static aeroelasticity

This field of study is concerned with the steady interaction between a fluid and a flexible structure. An example of this kind of problem is the bending and twisting of airplane wings in flight especially for long, slender structures as is shown in Figure 1.4.

Figure 1.4 NASA Helios, a solar powered prototype showing large deflection during flight [4]

Static aeroelastic analyses aim at determining the shape of a structure at different airflow conditions, which can impact the performance characteristics of the vehicle or help in optimizing the wing structure and shape. In addition, two other phenomena are of interest:

- Divergence, or static instability, occurs at high speed when the twist on the wing increases rapidly with airspeed and eventually leads to structural failure.

- Aileron-Reversal is a phenomenon that occurs at high speeds when the shifting of the center of pressure is combined with the elevated dynamic pressure to produce a resultant force that is greater than that generated by the deflection of the aileron. This is illustrated in Figure 1.5.

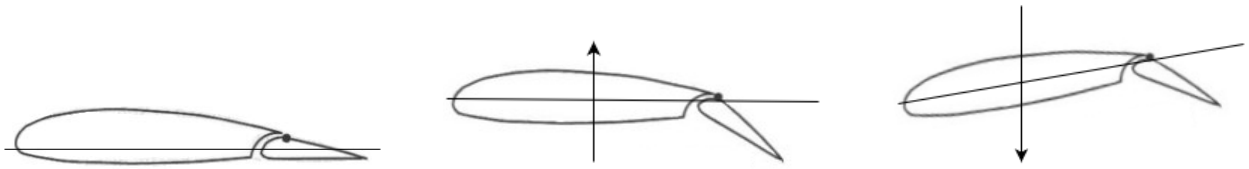

(a) (b) (c)

Figure 1.5 Aileron reversal (a) rigid wing at rest; (b) low airspeed with positive resultant force; (c) high airspeed with negative resultant force due to twisting of the section.

The coupled systems used to study this aspect of aeroelasticity are focused on determining the system of linear equations that emerges from the equilibrium of aerodynamic loads and the reaction attributed to deformation of the degrees-of-freedom. Several mathematical models exist for these phenomena, especially in two dimensions where representing the structural degrees-of-freedom is more straightforward. Thus, the use of numerical models is more common for problems in three dimensions or when nonlinearities are present, such as the effects of fluid viscosity and compressibility. Several nonlinearities can also be present in solid mechanics, such as the use of non-isotropic materials or geometrical nonlinearities (i.e. when the end-state differs significantly from the initial configuration of the problem, rendering the linear assumption and the principle of superposition inaccurate).

1.2.2 Dynamic aeroelasticity

The approach to unsteady problems is similar to the steady ones, with the specific characteristic that transient aerodynamics is a main driver of the behavior of the system. The study of dynamic aeroelasticity concentrates on two principal phenomena:

- Flutter, or dynamic instability, which is a divergent oscillation occurring when the damping of the dynamic system becomes negative.
- Gust alleviation or the behavior of the system when perturbed by short duration changes of the freestream conditions or atmospheric turbulence, which are usually random changes.

Because of pragmatic limitations, the amplitude of oscillations does not increase forever in the case of flutter and the system will reach structural failure [9]. This is why the velocity at which flutter happens is an important criterion for aircraft certification. In the presence of nonlinearities, this system will often reach limit-cycle oscillations (LCO), which is a periodic motion of constant amplitude.

1.3 Elements of the Problematics

In the field of aerospace, the processes of design and analysis are intrinsically multidisciplinary, such as when considering transonic and flexible aircraft wings [10]. The development of computational capabilities has and will continue to enable the development of high-fidelity Computational Fluid Dynamics (CFD) and Multidisciplinary Design Optimization (MDO). The latter's capabilities have considerably increased in recent years, to the point where its implementation is widespread among aircraft manufacturers and it is an active topic of research in academia.

On the other hand, as noted by [1], the complexity of the design process requires that multiple tools are integrated in an iterative fashion to leverage the intrinsic strengths of the various computational methods used, as well as the vast body of knowledge and skills accumulated by the engineers over the years.

These two factors show that there is a tension between low fidelity methods based on empirical data or simplified models that are able to provide results very quickly and high fidelity methods that provide superior insight into the physical problem and have the potential to greatly improve the end product at the cost of a much higher monetary and time investment.

The present research project inserts itself in between these two extremes by leveraging several low fidelity models into an integrated medium fidelity framework which extends the analytical capabilities at a significantly reduced cost compared to high fidelity methods.

Furthermore, moving toward an earlier integration of simulation into the design process can help optimize the designs and reduce development time and costs as was discussed in section 1.1. There is a need for the development of more accurate and complete analysis method to fill the gap between preliminary and detailed design. The proposed methodology also retains the segregated characteristic of the aerospace design process, where different disciplines are addressed with dedicated solvers.

Moreover, aeroelasticity has seen a resurgence of interest recently as modern aircraft design are more susceptible to encounter aeroelastic related phenomena in flight. First of all, the flexibility of aircraft wings has been increased by the use of lighter and stronger materials like

composites. Then, the aspect ratio of the wings is ever increasing in an attempt to reduce aerodynamic drag and obtain better performance for the same aircraft size. Also, better optimization and manufacturing techniques allow engineers to use smaller safety margins on the products they design or to better assess the uncertainty relating to their analyses. Finally, the commercial, and especially the business aviation market, apply pressure on the manufacturers to produce airplanes that can fly at a higher Mach number, thus increasing the aerodynamic loads and the importance of aeroelastic phenomena.

The relevance of this field and the need of novel approaches are examplified by the organization of the first and second Aeroelastic Prediction Workshops (AePW) by the American Institute of Aeronautics and Astronautics (AIAA) in 2013 and 2016 respectively. These workshops are an opportunity for the industry to bring forth and compare the state-of-the-art in the field and increase the technological readiness of the analysis methods.

1.4 Objectives

The main focus of this research is to develop numerical tools for the analysis of nonlinear aeroelastic coupling of aircrafts. An important aspect of the work is that it is applicable for the preliminary and conceptual phases of the design process. Therefore, the characteristics of the algorithms developed should be more towards robustness and automation at the expense of fidelity. Computational time is also an important factor, because the methods are aimed at providing insight into a large amount of possible configurations rather than a few detailed concepts.

1. Develop methods for static aeroelastic analysis of aircraft in the preliminary design phase.

2. Investigate the use of the previous framework for time domain coupled ODE problems of aircraft.

1.5 Thesis Outline

Firstly, a literature review explains the different analysis techniques related to aeroelasticity and their applications. Secondly, the techniques selected to be the most suited for the task at hand are explained into more details as well as their integration into a static aeroelasticity analysis framework. Then, the verification and validation of this framework is presented on several canonical and industrial test cases. The last theme will cover the work done in the coupling of forces in the time domain for two dimensional airfoils and for the flight

navigation of aircrafts in three dimensions. Lastly, a summary of the work is presented as well as recommendations for future developments.

CHAPTER 2 LITERATURE REVIEW

In this section, the concepts relating to aeroelasticity are explained in the following order: First, two-dimensional analysis of the system is shown to introduce the terminology and relevant definitions. Second, the different methods of determining the aerodynamic forces and mechanical deformations are looked at. Then, the coupling methodology of the two previous subjects and the issues that arise with this coupling are discussed. Lastly, an overview of the problematics and applications of aeroelastic studies is provided to highlight the trends in research and shed additional light on the choices made in the subsequent chapters.

2.1 Classical Wing Section (Theodorsen)

One of the earliest study of aeroelasticity applied to aeronautics is published in a paper by Theodorsen [11] in which the classical 2D airfoil section with a flap is defined. This work combines the thin-airfoil theory to compute unsteady aerodynamic forces integrated along the surface of the wing profile with the equations of motion for three degrees of freedom: heave, pitch, and flap. These variables are illustrated in Figure 2.1 and are denoted respectively by the variables h, the up and down motion of the section, α, the angle of attack of the entire section, and β, the angle of the control surface relative to the main profile. This definition is also used in reference works such as Dowell *et al.* [9] and De Langre [12].

The equations of motion comprise the reaction forces of the linear and rotational springs that are considered for each degree of freedom. The aerodynamic forces that cause a displacement are, respectively, the lift (L) and moments around α (M_α) and β (M_β) and the resulting system of linear equations corresponds to a three degree of freedom oscillator without damping, though extensions are possible to account for friction in the mechanisms.

The equations of motion for the system are listed in Eqs. (2.1) to (2.3), but the development and expression into a matrix form suitable for numerical resolution in the time domain are shown in Appendix A. The equations use the distances a, b, c, x_α, and x_β marked in Figure 2.1 as well as the mass (M), moment of inertia (I), and the static moment of inertia (S) for each degree of freedom. Finally, the stiffness associated with each degree of freedom are represented by K_h, K_α, K_β.

$$M\ddot{h} + S_\alpha\ddot{\alpha} + S_\beta\ddot{\beta} + K_h h = L \tag{2.1}$$

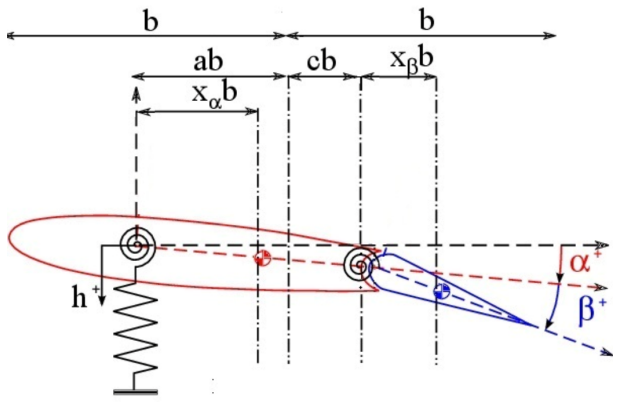

Figure 2.1 Definition of variables and coordinates for the 3 degrees-of-freedom classical section in 2D

$$S_\alpha \ddot{h} + I_\alpha \ddot{\alpha} + K_\alpha \alpha + I_\beta \ddot{\beta} + b(c-a)S_\beta \ddot{\beta} = M_\alpha \tag{2.2}$$

$$S_\beta \ddot{h} + I_\beta \ddot{\alpha} + b(c-a)S_\beta \ddot{\alpha} + I_\beta \ddot{\beta} + b(c-a)S_\beta \ddot{\beta} + K_\beta \beta = M_\beta \tag{2.3}$$

This system is also sometimes simplified by removing the flap, thus allowing only heaving and pitching motion. It is also important to note that the aerodynamic assumptions used by Theodorsen constrain the problem to linear, inviscid, incompressible, and irrotational flows, as well as low amplitude and periodic motions. Several extensions have been proposed to this problem since and are listed with a brief description of their focus and contributions below.

The generalization of unsteady aerodynamics to arbitrary motion is done in Edwards *et al.* [13]. Also, aerodynamic modifications have been proposed by several authors such as Marzocca *et al.* [14] who modified the unsteady loads to better approach the experiments in different flight regimes from subsonic to supersonic. The work of Yang *et al.* [15] compared the classical aerodynamic theory with results obtained from solving the Euler equations for subsonic flow conditions.

Other authors have looked at the freeplay nonlinearity in the pitching stiffness both experimentally [16] and numerically [17, 18]. Also, Tang *et al.* [19] as well as Trickey *et al.* [20] applied similar techniques to solve the nonlinearity problem in three degrees of freedom problems where the flap is experiencing nonlinearities such as freeplay. A study by Zhao & Hu [21] used the Vortex Lattice Method (VLM) to also look into the behavior of nonlinear two degrees of freedom systems.

Another nonlinearity commonly studied is the cubic hardening, in which the stiffness of one of the degrees of freedom is not purely linear but varies with deflection by a third degree law. The effects related to wing and section flexibility have also been shown to have an effect on the flutter characteristics of the system [22].

Overall, the Theodorsen model is still a useful model to understand the relationships between aerodynamic, inertial, and structural forces on airplane wings.

2.2 Aerodynamic Analysis Methods

The determination of wing loading can be done by using several methods ranging from low to high fidelity. Figure 2.2 shows the different aerodynamic computational models and their differences. The aim of the current section is to briefly introduce the various computational methods and locate the present research project accordingly. Details of implementation and numerical resolution are not discussed in detail here, but rather in the following chapter.

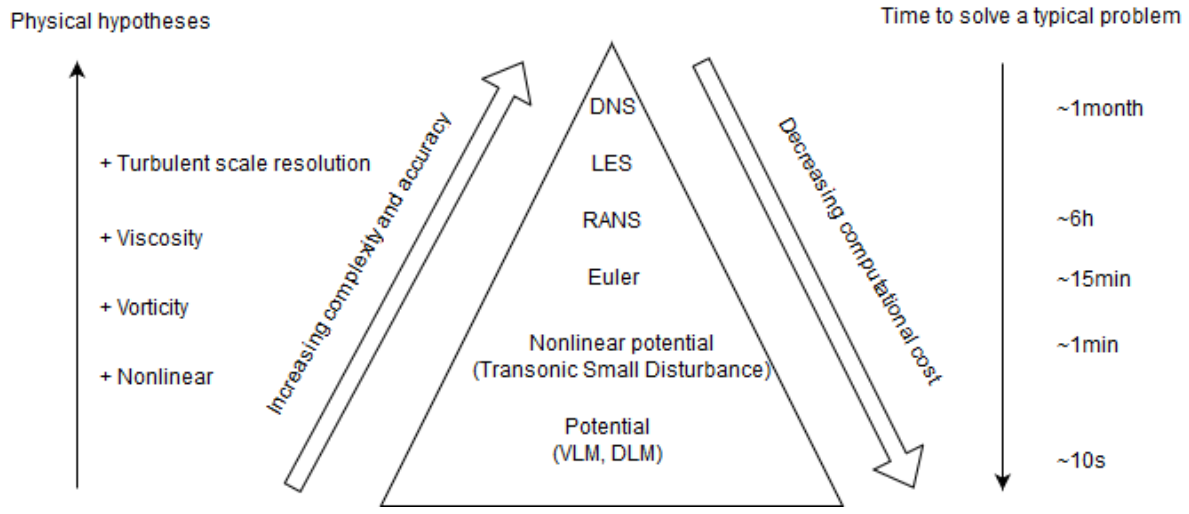

Figure 2.2 Hierarchy of fluid flow models arranged by complexity (fidelity) and computational cost

Direct Numerical Simulation (DNS) is currently the most physically accurate resolution methods of aerodynamic problems. It consists in solving the Navier-Stokes equations directly, without turbulence model, but this imposes the use of a very fine mesh to capture every continuous physical phenomena with the discrete approximation and a very small timestep to capture the unsteady part of the airflow. The Navier-Stokes equations taken from Anderson [23] are listed in Eqs. (2.4) to (2.6) for reference.

Continuity:

$$\frac{\partial \rho}{\partial t} + \nabla \cdot \rho V = 0 \tag{2.4}$$

Momentum:

$$\rho \frac{Du}{Dt} = -\frac{\partial p}{\partial x} + \frac{\partial \tau_{xx}}{\partial x} + \frac{\partial \tau_{yx}}{\partial y} + \frac{\partial \tau_{zx}}{\partial z} \tag{2.5a}$$

$$\rho \frac{Dv}{Dt} = -\frac{\partial p}{\partial y} + \frac{\partial \tau_{xy}}{\partial x} + \frac{\partial \tau_{yy}}{\partial y} + \frac{\partial \tau_{zy}}{\partial z} \tag{2.5b}$$

$$\rho \frac{Dw}{Dt} = -\frac{\partial p}{\partial z} + \frac{\partial \tau_{xz}}{\partial x} + \frac{\partial \tau_{yz}}{\partial y} + \frac{\partial \tau_{zz}}{\partial z} \tag{2.5c}$$

Energy:

$$\begin{aligned} \rho \frac{D(e + V^2/2)}{Dt} &= \rho \dot{q} + \frac{\partial}{\partial x}(k \frac{\partial T}{\partial x}) + \frac{\partial}{\partial y}(k \frac{\partial T}{\partial y}) + \frac{\partial}{\partial z}(k \frac{\partial T}{\partial z}) - \nabla \cdot pV \\ &+ \frac{\partial u \tau_{xx}}{\partial x} + \frac{\partial u \tau_{yx}}{\partial y} + \frac{\partial u \tau_{zx}}{\partial z} + \frac{\partial v \tau_{xy}}{\partial x} + \frac{\partial v \tau_{yy}}{\partial y} + \frac{\partial v \tau_{zy}}{\partial y} + \frac{\partial w \tau_{xz}}{\partial x} + \frac{\partial w \tau_{yz}}{\partial y} + \frac{\partial w \tau_{zz}}{\partial z} \end{aligned} \tag{2.6}$$

In these equations, the variables u, v, w stand for the components of the velocity vector V, ρ is the density of the fluid, p is the pressure, and τ is the shear force acting on the fluid element. The energy equation contains more variables, among which are the temperature of the fluid T, its thermal conductivity k, the heat generation per unit volume $\dot{q}$, and the internal energy e.

Large Eddy Simulation (LES) is another high-fidelity fluid dynamics computational method where the largest turbulent structures of the flow are resolved explicitly, analogous to DNS, and the smallest details are approximated by using a Subgrid Scale (SGS) Model. This reduces the computational cost slightly while still allowing superior resolution in the solution domain.

The Reynolds-Averaged Navier-Stokes (RANS) equations are currently what is referred as high fidelity in the aerospace industry, as the DNS and LES methodologies are too costly to have pragmatic applications in the design of aircrafts. It consists in taking the time averaged equations of fluid flow where the small scale unsteadiness of the flow can be approximated with various turbulence models. The most common turbulence models vary depending on the application, but for external aerodynamics the Spalart-Allmaras one-equation model [24] is one of the most commonly used.

The Euler equations are essentially the same as the Navier-Stokes equations with the difference that fluid viscosity is neglected, leaving the inviscid and compressible continuity,

momentum, and energy equations. In an industrial context, this methodology is often considered medium fidelity as it significantly reduces the computational cost compared to RANS simulations, but the physical representation of nonlinear phenomena such as oblique shock at transonic speed does not match the experiments closely. It is possible to apply corrections based on empirical or experimental knowledge, but these techniques are now superseded by the RANS solvers. The inviscid equations are Eqs. (2.7) to (2.8) [23], with the continuity equation being the same as Eq. (2.4):

Momentum:

$$\rho\frac{Du}{Dt} = -\frac{\partial p}{\partial x} + \rho f_x \tag{2.7a}$$

$$\rho\frac{Dv}{Dt} = -\frac{\partial p}{\partial y} + \rho f_y \tag{2.7b}$$

$$\rho\frac{Dw}{Dt} = -\frac{\partial p}{\partial z} + \rho f_z \tag{2.7c}$$

Energy:

$$\rho\frac{D(e+V^2/2)}{Dt} = \rho\dot{q} - \nabla\cdot pV + \rho(f\cdot V) \tag{2.8}$$

Then, there are resolution methods based on the potential equations or the linearized versions of these equations which consider the compressibility of the airflow in the form of a dependence on the Mach number, with the linear equations possessing a singularity when $M = 1.0$. These two formulations are presented in Anderson [23] as well as Cebeci *et al.* [25]. The potential equation emerges by defining a velocity potential (ϕ) for steady, irrotational, isentropic flow where $\mathbf{V} = \nabla\phi$. This assumption allows to simplify the equations of fluid flow to obtain the nonlinear partial differential equation expressed in Eq. (2.9) for two dimensional flow.

$$[1 - \frac{1}{a^2}(\frac{\partial\phi}{\partial x})^2]\frac{\partial^2\phi}{\partial x^2} + [1 - \frac{1}{a^2}(\frac{\partial\phi}{\partial y})^2]\frac{\partial^2\phi}{\partial y^2} - \frac{2}{a^2}(\frac{\partial\phi}{\partial x})(\frac{\partial\phi}{\partial y})\frac{\partial^2\phi}{\partial x\partial y} = 0 \tag{2.9}$$

where a is the speed of sound. This equation is usually solved by using finite difference techniques. The linearized version of this equation is found by posing a uniform flow and solving only for the perturbation velocity defined in Eq. (2.10).

$$\phi = V_\infty x + \hat{\phi} \tag{2.10}$$

with the freestream velocity V_∞ being oriented exclusively in the x direction and the perturbation velocity potential being $\hat{\phi}$. Which gives, when substituting in the previous equation,

Eq. (2.11) for the small disturbance potential equation.

$$(1 - M_\infty^2)\frac{\partial^2 \hat{\phi}}{\partial x^2} + \frac{\partial^2 \hat{\phi}}{\partial y^2} = 0 \tag{2.11}$$

We conclude the overview of aerodynamics analysis methods with the linear potential category, mostly constituted by panel methods, which are among the lowest fidelity aerodynamics computational codes. They are based on singularities, elementary solutions to the potential equation 2.12, such as the doublet for the Double-Lattice Method (DLM) or the vortex ring for the Vortex-Lattice method (VLM). Both methods are equivalent [5], although their implementation varies slightly which makes the DLM usually preferred for frequency domain computations and VLM, or its unsteady version UVLM, more common for time domain solutions. They both function in the same way: the solutions are constructed as a superposition of elementary flow solutions distributed on the surface of the object analyzed. These computational methods are classified as low fidelity.

$$\nabla^2 \phi = 0 \tag{2.12}$$

Inviscid and incompressible flow hypotheses are used to develop these formulations, but there are various ways of introducing flow nonlinearities. One of them is to apply a correction to the Aerodynamic influence matrix of the DLM [26] for viscosity and compressibility effects. The main drawback of these methods is that they rely on performing higher-fidelity computations on the current configuration, which is not very practical in the earliest design stages, or to use extrapolations based on previous knowledge about the appropriate corrections. The VLM formulations can be corrected with similar effects by comparing to a CFD database or flight test data [27, 28].

In the current research project, the latest approach is used to combine the three dimensionality and low computational cost of the VLM with the viscous and compressible nonlinearities captured by RANS simulations. To keep the computational cost low, the RANS simulations are performed on a quasi 3D flow solver making it much faster and more robust than a fully 3D RANS case. The details of its implementation into an inhouse CFD solver is presented in Parenteau *et al.* [7].

2.3 Structural Analysis Methods

Static structural analysis methods are numerical methods to solve a linear elastic problem that can be stated by Hooke's law as follows:

$$F = Kx \tag{2.13}$$

where F represents the load applied on the structure, x is the deformation experienced, and K is the proportionality constant, also called stiffness.

Analytical or empirical solutions for the deformation of structures are found for simple geometries and load cases, but they quickly become unattainable for more complex geometries and require the use of numerical resolution.

The finite element method (FEM) is a discrete solution method where the combination of various element formulations is used to constitute a global stiffness that relates the loading and the displacement of every degree of freedom on the structure [29, 30].

As was discussed previously, the level of details required for the structural analysis of an aircraft wing depends greatly on the goals of the design phase reached until that point. Therefore, a great range of complexity exists in the representation of the wing either as a simple beam ($\approx \sigma(10^2)$ elements) or a three dimensional assembly of pieces ($\approx \sigma(10^6)$ elements). The Finite element method is suitable for this kind of applications as it allows the use of various element types (like bars, shells, and prisms) and even higher order elements.

The use of volumetric finite element models in aerospace is reserved for the detailed analysis because of the complexity of the product and the computational cost associated.

Beam models, also called stick models in some references, consist in reducing the number of degrees of freedom to the point where only one dimension is significant. This has many applications in aerospace such as the use of Euler-Bernoulli beam formulations to solve the deflections in flight. Studies such as Elsayed *et al.* [31] focus on developing and comparing reduced order models, such as stick models, to represent the structure of aircraft wings. Another study reported by Bdeiwi *et al.* [32] compared the beam model with 3D finite element meshes to conclude that both models performed similarly in predicting the static aeroelastic deflection of aircrafts.

Another approach with beam models is the geometrically nonlinear beam theory [33], where the time derivatives of the degrees of freedom are explicitly resolved to account for nonlinear unsteady behavior. This method has the advantage of being more accurate where beams are suitable, but is difficult to generalize in three dimensions and is therefore limited in its applications. The study of large deformation but small strain beam elements has also been performed by Hsiao *et al.* [34, 35] and Benerjee *et al.* [36].

2.4 Aeroelastic Coupling

The coupling of computational fluid dynamics and solid mechanics problems can be done with a monolithic (or strongly coupled) algorithm, where the coupled structural and aerodynamic equations are solved jointly. The alternative is a staggered (or loosely coupled) algorithm [37]. In the case of static aeroelasticity, the difference is irrelevant as there is no timestepping involved.

The staggered approach is more easily implemented as it can build on pre-existent separate solvers for the fluid and structure and is less computationally costly than the coupled system. The main drawback is that the solution convergence is limited to first order even though the underlying solvers are second-order accurate in space and time [38].

Another approach, confusingly referred to as strongly coupled by certain authors, consists in solving the staggered problem iteratively for every timestep until convergence is reached and this allows to regain the higher accuracy orders that are prohibited by the loosely coupled algorithms.

The staggered algorithms also require the interpolation of forces from the aerodynamic solution to the structural mesh and the reverse for the displacements. This has lead to research on interpolation algorithms that are robust, simple, and accurate. A conservative interpolant approach is proposed by Farhat *et al.* [39]. In this method the connectivity between the coarse and the fine mesh is done ad-hoc, by using a search algorithm or the equivalent. Other authors have used Radial Basis functions [40] as a mean of making this interpolation more robust, more accurate, and faster.

The commonly used structural solver NASTRAN supports the use of splines, either 1D curves or 2D surfaces that are used as the basis for the connectivity of the aerodynamic and the structural meshes. A similar approach was used in the current project with the developments by Farhat *et al.* [39] being incorporated also in an inhouse FEM solver. The details of its implementation are presented by Grozdanov [41].

2.5 Aeroelastic studies

The literature has many examples of studies in the field of aeroelasticity. These span, almost chronologically, 2D airfoils, 2D airfoils-aileron systems, 3D wings, and 3D wings with fuselage and horizontal/vertical tail configurations. In parallel, the methods used are a combination of the previously mentioned aerodynamics, structural, and aeroelastic coupling spread in various groups of fidelity levels depending on the scope of the individual studies. The aim of

this section in contrast to the previous ones is to tie together the various topics covered and establish the relevance of the proposed approach.

Low fidelity methods such as Vortex Lattice Method (VLM) and structural beam models have recently been used to predict the aeroelastic behavior and flight performance of High-Altitude Long-Endurance (HALE) aircrafts [42, 43]. These test cases provide an interesting proving ground for these techniques because the cruise speed is usually subsonic, so potential flow approximations are suitable, and the very high aspect-ratio of the wings reduces the importance of three dimensional aerodynamic effects. Furthermore, those aircrafts are susceptible to very large deflections of their planform, which makes the consideration of non-linear structural effects necessary. A good overview of the state of the art in the field of aeroelasticity of high-aspect ratio vehicles is provided by Afonso *et al.* [44]. Many different authors have also contributed to the subject, as shown in Table 2.1.

Other higher fidelity studies exist but the results do not warrant the increase in computational time as they are comparable to lower fidelity methods most of the time [32]. Other notable references have performed high fidelity static aeroelastic computations on aircrafts, such as Keye *et al.* [45, 46] on the NASA CRM and the DLRF6 airplanes, hantrais-Gervois *et al.* [47] have used 3D RANS and FEM models to study the control surface effectiveness at high speed, and a test case for the Aeroelastic prediction workshop is presented by Chwalowski *et al.* [48].

Table 2.1 Roadmap of aeroelastic studies in the literature

	Low Fidelity	Medium Fidelity	High fidelity
Simple topology (wings)	Arena (2013) [49], de Souza (2012) [50], Murua (2012) [51], Murua (2012) [43], Nguyen (2017) [52], Patil (1998) [53], Smith (2001) [42], Spada (2014) [54], Spada (2014) [55], Simpson (2013) [56], Simpson (2017) [57], Palacios (2010) [58], Paul (2014) [59], Simpson (2013) [60]	Guruswamy (19880 [61], Mantegazza (1990) [62], Andersen (1998) [63], Eastep (2001) [64], Eastep (2009) [65],	Kim (2013) [66], Yoon (2012) [67]
Complex topology (aircrafts)	Afonso (2017) [44], Mauermann (2011) [68],		Bdeiwi (2019) [32], Keye (2013) [46], Keye (2011) [45], Keye (2009) [69], Keye (2014) [70] Hernandez (2018) [71]

Furthermore, many publications study the issues related to MDO and the integration of aeroelasticity in optimization frameworks : [72], [73], [74], [75], [76], [77], [1]. These publications tend to vigorously prefer the use of staggered approach and dedicated solvers for every discipline based on the historic of developments of these codes in the organization, as well as the reduced complexity of this approach making it more easily manageable.

CHAPTER 3 STATIC AEROELASTICITY ANALYSIS FRAMEWORK

This chapter details the various methodologies employed to perform the simulations in chapter 4. Since the work is based on previously developed analysis tools such as the VLM with viscous correction, these are discussed with focus on specific details affecting the aeroelastic framework rather than an exhaustive presentation of the entire implementation.

3.1 Finite Element Solver

The current section details the resolution methodology for the solid mechanics part of the aeroelastic solver. The solution is obtained via the finite element method, which consists in representing the problem as an assembly of *finite elements* with various boundary conditions applied at the nodes. In this framework, beam elements are used and this section first explains the development of stiffness matrices for the Beam finite element and, then, the linear and nonlinear solution algorithms.

3.1.1 Beam element model

The stiffness matrix of the elements allows to relate the loads applied at the nodes to their displacements. The formulation of the element determines its stiffness matrix, which is local to the element. The next step is to assemble the problem into a global system of linear equations by connecting every element, which requires transforming the local stiffness matrix into global coordinates.

Beam elements

For an isotropic material not experiencing plastic deformation, the stress-strain relationships are simple relations: Eq. (3.1) presents the relation in the case of linear stresses and Eq. (3.2) shows the case of shear stresses.

$$\epsilon_x = (\sigma_x - \nu(\sigma y + \sigma z))/E \tag{3.1a}$$

$$\epsilon_y = (\sigma_y - \nu(\sigma x + \sigma z))/E \tag{3.1b}$$

$$\epsilon_z = (\sigma_z - \nu(\sigma x + \sigma y))/E \tag{3.1c}$$

$$\gamma_{xy} = \frac{\tau_{xy}}{G} \tag{3.2a}$$

$$\gamma_{yz} = \frac{\tau_{yz}}{G} \tag{3.2b}$$

$$\gamma_{xz} = \frac{\tau_{xz}}{G} \tag{3.2c}$$

Where E is Young's modulus, ν is Poisson's ratio, and $G = E/(2(1+\nu))$ is the shear modulus. This is often expressed in matrix form shown in Eq. (3.3)

$$\begin{pmatrix} \epsilon_x \\ \epsilon_y \\ \epsilon_z \\ \gamma_{xy} \\ \gamma_{yz} \\ \gamma_{xz} \end{pmatrix} = \frac{1}{E} \begin{bmatrix} 1 & -\nu & -\nu & & & \\ -\nu & 1 & -\nu & & & \\ -\nu & -\nu & 1 & & & \\ & & & 2(1+\nu) & & \\ & & & & 2(1+\nu) & \\ & & & & & 2(1+\nu) \end{bmatrix} \begin{pmatrix} \sigma_x \\ \sigma_y \\ \sigma_z \\ \tau_{xy} \\ \tau_{yz} \\ \tau_{xz} \end{pmatrix} \tag{3.3}$$

Although a more useful expression is the reciprocal of this, shown in Eq. (3.4), expressing the stress vector as a function of the strains. The development of this matrix, called the compliance matrix, from the normal and shear stress relationships is shown in appendix B.

$$\begin{pmatrix} \sigma_x \\ \sigma_y \\ \sigma_z \\ \tau_{xy} \\ \tau_{yz} \\ \tau_{xz} \end{pmatrix} = \frac{E}{(1+\nu)(1-2\nu)} \begin{bmatrix} 1-\nu & \nu & \nu & & & \\ \nu & 1-\nu & \nu & & & \\ \nu & \nu & 1-\nu & & & \\ & & & \frac{1}{2}-\nu & & \\ & & & & \frac{1}{2}-\nu & \\ & & & & & \frac{1}{2}-\nu \end{bmatrix} \begin{pmatrix} \epsilon_x \\ \epsilon_y \\ \epsilon_z \\ \gamma_{xy} \\ \gamma_{yz} \\ \gamma_{xz} \end{pmatrix} \tag{3.4}$$

Or

$$\vec{\sigma} = [S]\vec{\epsilon} \tag{3.5}$$

For a given element shape, strain-displacement relation are found to correlate the strain previously introduced to the nodal displacements of the elements. To do so, the element's shape functions are used to interpolate the strain inside the elements domain from nodal values, finite elements are a piecewise continuous approximation of the solution. In this case, the shape functions are chosen for a two-node Euler-Bernoulli beam element. The degrees of freedom can be separated in three separate loading types: Axial deformation are related to

tension and compression loads; rotation of the axis of the beam are caused by torsion of the beam; and bending deformations are a combination of transverse displacement and rotation resulting from lateral forces and bending moments.

Because the first two deformations are simple coupling of corresponding degrees of freedom, the shape functions are linear. Figure 3.1 shows the axial displacements u_1 and u_2. From this sketch, it is easy to see that the axial displacement at every point of the beam's axis is represented by Eq. (3.6) where x is the position at which the displacement is evaluated and L is the initial length of the beam.

$$u_x = u_1 + (u_2 - u_1)\frac{x}{L}) \tag{3.6}$$

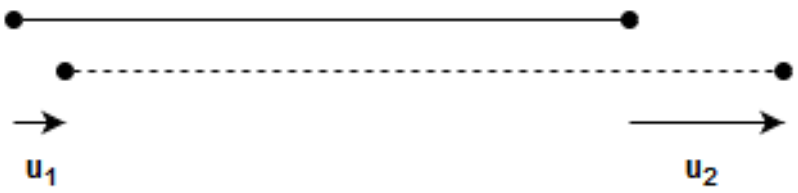

Figure 3.1 Linear beam axial displacements

This can also be expressed in the following form (Eq. (3.7)), from which the shape functions (N_1 and N_2) are more apparent. These same shape functions are used for the interpolation of loads discussed in section 3.3, see Figure 3.9.

$$u_x = u_1(1 - \frac{x}{L}) + u_2\frac{x}{L} = N_1u_1 + N_2u_2 \tag{3.7}$$

The same process and same shape functions are applicable for the representation of torsional displacements. Due to the coupling between transverse displacements and rotations, the shape functions for bending takes a third degree polynomial form as can be seen on Figure 3.2. This leads to the continuous form for the deformation of the neutral axis to take the shape of Eq. (3.8) where the shape functions are expressed in Eq. (3.9) ([29]). It is important to note that these equations and figures are in 2D, where bending in the xy plane is such that $u_1 = y_1$, $u_2 = \theta_{z,1}$, $u_3 = y_2$, $u_4 = \theta_{z,2}$. Bending in the perpendicular plane xz functions in the same way, but $u_1 = z_1$, $u_2 = -\theta_{y,1}$, $u_3 = y_2$, $u_4 = -\theta_{y,2}$.

$$u_y = N_1u_1 + N_2u_2 + N_3u_3 + N_4u_4 \tag{3.8}$$

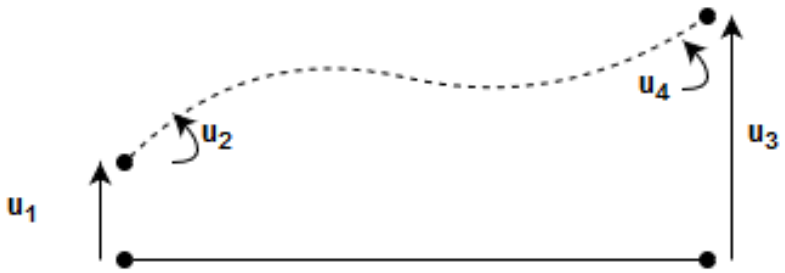

Figure 3.2 Linear beam transverse displacements

$$N_1 = 1 - \frac{3x^2}{L^2} + \frac{2x^3}{L^3} \tag{3.9a}$$

$$N_2 = x - \frac{2x^2}{L} + \frac{x^3}{L^2} \tag{3.9b}$$

$$N_3 = \frac{3x^2}{L^2} - \frac{2x^3}{L^3} \tag{3.9c}$$

$$N_4 = -\frac{x^2}{L} + \frac{x^3}{L^2} \tag{3.9d}$$

To summarize, the shape functions establish relations between the values at the nodes and the same quantities inside the domain of the beam. An important derivation of this is made between the displacements at the nodes and the strains of the beam. In general, Eq. (3.10) and Eq. (3.11) are the standard definitions of the axial and shear strain.

$$\epsilon_{ii} = \frac{\partial u_i}{\partial x_i} \tag{3.10}$$

$$\gamma_{ij} = \frac{\partial u_i}{\partial x_j} + \frac{\partial u_j}{\partial x_i} \tag{3.11}$$

A matrix B is then defined that contains the derivatives of the shape functions already stated for all displacements at the nodes in order to correlate the 6 components of strain and all the displacements at the nodes. Because each node contains 6 degrees of freedom, the relationship between displacements and strains takes the form of Eq. (3.12).

$$\epsilon_6 = [B]_{6x12}\mathbf{u}_{12} \tag{3.12}$$

The stiffness matrix is then computed from the potential energy of the beam stated in Eq. (3.13).

$$U = \frac{1}{2}\mathbf{u}^T\mathbf{K}\mathbf{u} \tag{3.13}$$

Or from the integration of the strain energy in the entire beam, the following Eq. (3.14) is also true.

$$U = \frac{1}{2}\int_\Omega \sigma^{\mathbf{T}}\epsilon \; d\Omega \tag{3.14}$$

With the stress-strain relationships already presented in Eq. (3.5).

$$U = \frac{1}{2}\int_\Omega \epsilon^T \; \mathbf{S} \; \epsilon \; d\Omega \tag{3.15}$$

And by introducing Eq. (3.12).

$$U = \frac{1}{2}\mathbf{u}^T \int_\Omega \mathbf{B}^T \; \mathbf{S} \; \mathbf{B} \; d\Omega \; \mathbf{u} \tag{3.16}$$

and

$$\mathbf{K} = \int_\Omega \mathbf{B}^T \; \mathbf{S} \; \mathbf{B} \; d\Omega \tag{3.17}$$

3.1.2 Linear solution

The structural modeling of the wing was done through an in-house finite element solver (OFEM) that allows the resolution of problems involving geometrical nonlinearities such as large deformations of slender beams. It solves the displacement based finite element equations [29].

The solution method for linear problems is obtained by solving Eq. (3.18), where K represents the global stiffness matrix of the problem, D the displacement vector and R the force vector.

$$[K]D = R \tag{3.18}$$

This can be summarized by algorithm 1:

The linear displacement of a cantilever beam depends only on the initial position and applied forces. This is evidently a first order approximation when the displacement is enlarged (see figure 3.3). This leads to an unnaturally large increase in the beam's length that can become a problem if the beam represents an aircraft wing. The increase in length of the planform

Algorithm 1 Linear Structural deflection

Compute the local stiffness matrix for each element
Rotate the local stiffness matrix from the local to the global coordinate system
Assemble the Global stiffness matrix $[K]$
Solve the linear system of equations for the unknown displacements $x = [K]^{-1}F$

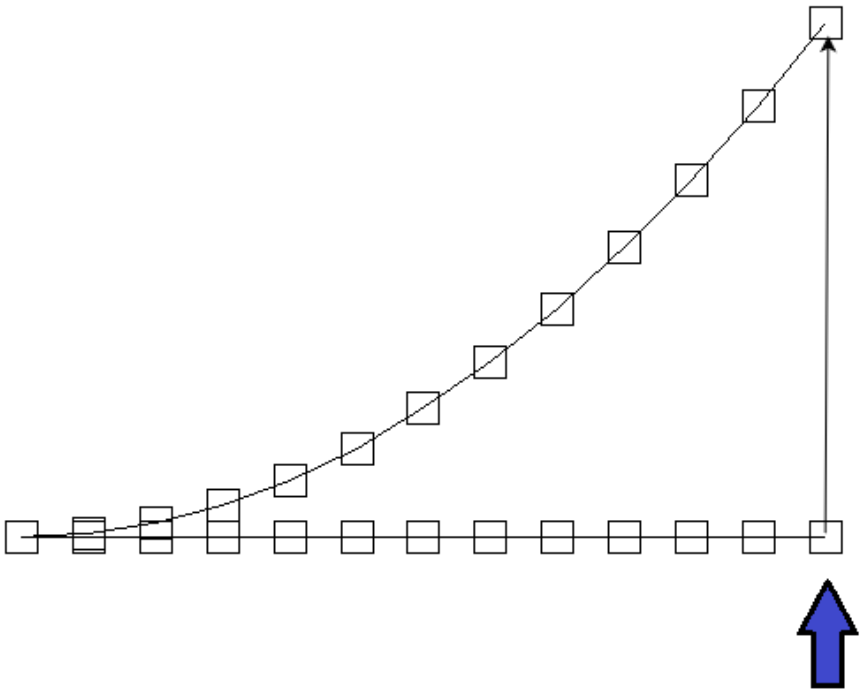

Figure 3.3 Linear beam displacement for a cantilever beam in bending

will result in a proportional increase in lift, which will in turn cause more deflection and the numerical solution to aeroelastic system will be off by a significant margin. This is why the geometrically nonlinear resolution was implemented and is used on all static aeroelastic problems in this document.

3.1.3 Nonlinear solution

The nonlinear solution method solves the elasticity equation iteratively by the Newton-Raphson algorithm, also called load-imbalance method. The problem is first solved with a linear step, then the internal forces R^{int} are computed with the displacement vector at the previous iteration and the local stiffness matrix of each element. The residual is then found

by using equation 3.20.

$$R^{int} = \sum_{n=1}^{N_{elements}} [K_{local}] D_{local} \tag{3.19}$$

$$R^{res} = R^{ext} - R^{int} \tag{3.20}$$

The global stiffness matrix is then recalculated using the new position of each elements, i.e. a rotation of every local coordinate system is performed, and the next step i is expressed as

$$[k]^i \Delta D^i = R^{res,i} \tag{3.21}$$

Algorithmically, this process can be expressed as follows:

Algorithm 2 Nonlinear Structural deflection

Compute the local stiffness matrix for each element
while $\Delta D^i > \epsilon$ **do**
    Rotate the local stiffness matrix from the local to the global coordinate system
    Assemble the Global stiffness matrix $[K]$
    Compute the internal forces and the load imbalance residual $R^{res} = R^{ext} - R^{int}$
    Solve the linear system of equations for the unknown displacements $[k]^i \Delta D^i = R^{res,i}$
end while

If we come back to the previously shown cantilever beam in bending, we can see how the iterative procedure corrects the solution. The initial displacements were parallel to the applied force, which resulted in an elongation of the beam. Slender beams usually have much higher axial stiffness compared to the transverse, which explains why the computed internal forces have a strong axial component. This results in a net force that causes the displacements to slightly contract the beam, as is shown in figure 3.4. It can also be noticed that the overall displacement of the nodes is much smaller than the initial displacement, which shows that the algorithm can converge.

In theory, this iterative procedure could be unstable or oscillations could cause the convergence to be prohibitively slow. However, in the type of cases that are typical of an airplane lifting surface, only geometrical nonlinearities are present due to the large deformations of the wing and the stiffness of the elements is linear throughout the computation, which does not pose any problem. It is noted in [29] that for problems involving nonlinear stiffness this type of numerical issues should be addressed. Nevertheless, to make sure the algorithm is stable, a numerical relaxation factor is applied on the computed displacement increment of

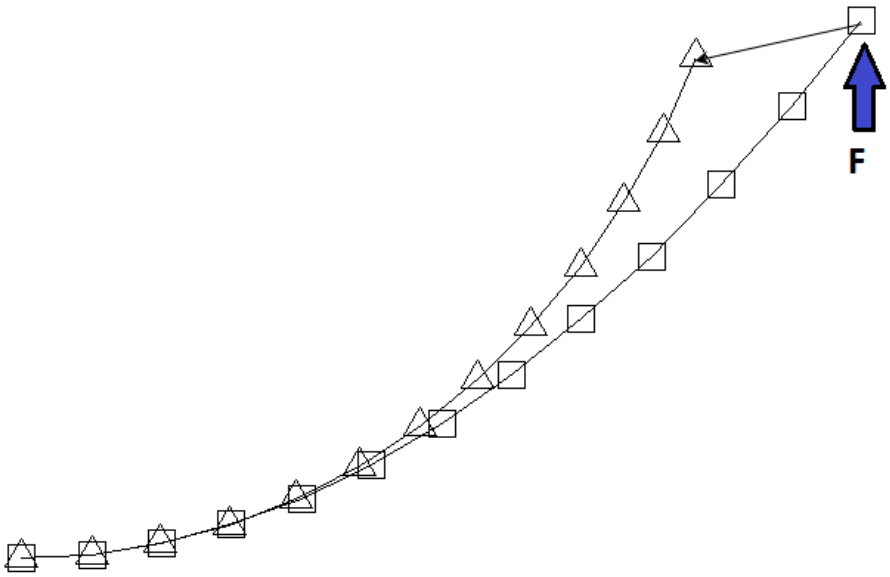

Figure 3.4 Nonlinear beam displacement for a cantilever beam in bending

the form:

$$\Delta D^i = \Delta D^i \cdot \chi \tag{3.22}$$

with $0 \leq \chi \leq 1$

3.2 Vortex-Lattice Method

This section explains the medium fidelity aerodynamics load computation tool based on the Vortex Lattice Method with correction taken from a 2.5D RANS database.

3.2.1 Potential Formulation

The Vortex Lattice Method is a low fidelity method that represents the wing's complex geometry by only its planform, thus achieving low computational time. The implementation used is based on the presentation by Katz & Plotkin [5]. In this method, the wing is replaced by an array of panels representing bound vortices or vortex rings as shown in Figure 3.5.

Each panel comprises a collocation point at its center on which the influence of every other panel is computed using the Biot-Savart law (Eq. (3.23)).

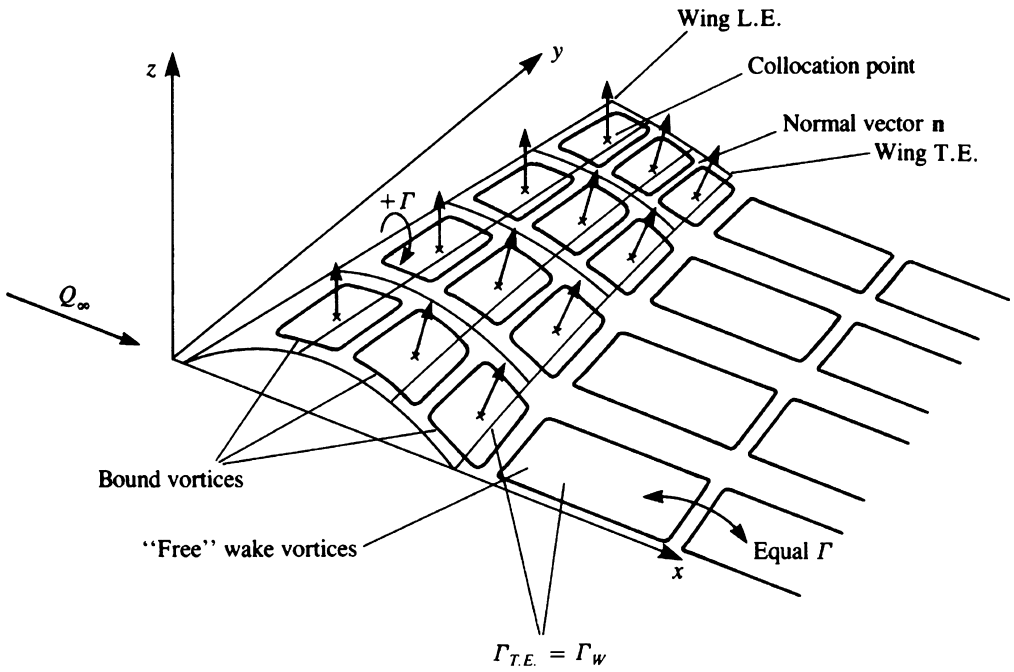

Figure 3.5 Representation of a lifting surface using the vortex rings [5]

$$\delta q = \frac{\Gamma}{4\pi}\frac{d\vec{l}\times\vec{r}}{r^3} \tag{3.23}$$

Where V is the velocity potential in the potential equation (Eq. (2.12)), Γ is the strength of the vortex element, $d\vec{l}$ is the infinitesimal vortex element, and $\vec{r}$ is the distance between the vortex element and the evaluation point. This enables the construction of a linear system of equations where the unknowns are the strength of every vortex (Γ) of the form:

$$[A]\Gamma = RHS \tag{3.24}$$

or in its developed form:

$$\begin{bmatrix} A_{11} & A_{12} & \dots & A_{1n} \\ A_{21} & A_{22} & \dots & A_{2n} \\ \vdots & \vdots & \ddots & \vdots \\ A_{n1} & A_{n2} & \dots & A_{nn} \end{bmatrix} \begin{pmatrix} \Gamma_1 \\ \Gamma_2 \\ \vdots \\ \Gamma_n \end{pmatrix} = \begin{pmatrix} RHS_1 \\ RHS_2 \\ \vdots \\ RHS_n \end{pmatrix} \tag{3.25}$$

With the aerodynamic influence coefficients (A_ij) being computed using the Biot-Savart law Eq. (3.23).

The right hand side of the equation (RHS) contains the boundary conditions of the problem. First, the non-penetration condition on every collocation point is enforced (Neumann boundary condition). This is represented by the scalar product of the freestream velocity and the normal vector of each panel, see equation 3.26. The last boundary condition stipulates that, at the trailing edge, the vorticity jump must be zero to satisfy the smooth change in velocity, also called the Kutta-Joukowski condition. This is shown on Figure 3.5 by the statement $\Gamma_{T.E.} = \Gamma_W$ and is implemented implicitly by adding the influence of the wake panels with the strength of the corresponding trailing edge panel in the influence matrix A.

$$RHS_i = -\vec{\mathbf{U}}_\infty \cdot \vec{\mathbf{n}}_i \tag{3.26}$$

The Vortex Lattice Method is a linear potential method, it is therefore only suitable for incompressible, inviscid, and attached airflows. The nonlinearities associated with these physical phenomena are introduced through the viscous coupling explained in the next section.

Once the strength of every vortex panel has been solved, the forces can be computed by using equation 3.27 for the leading edge panel and equation 3.28 for all other panels.

$$L_i = \rho U_\infty(\Gamma_i)\delta y \tag{3.27}$$

$$L_i = \rho U_\infty(\Gamma_i - \Gamma_{i-1})\delta y \tag{3.28}$$

Where ρ is the air density, U_∞ is the freestream flow, δy is the width of the panel perpendicular to , Γ_i is the vortex strength of the current panel, and Γ_{i-1} is the vortex strength of the panel directly upstream. The total lift of the surface is found by summing the lifting force of all the panels. Note that the lift, expressed this way, is perpendicular to the freestream by definition, as the equation contains only scalars.

3.2.2 Viscous Coupling

The methodology used in the project is presented in details in Parenteau *et al.* [78]. The main lines are presented here to introduce the reader to the methodology and the implications they have on the aeroelastic framework. First, the 2.5D RANS solver used to generate the aerodynamic force coefficient database is presented, followed by the Nonlinear VLM coupling algorithm.

2.5D RANS solver

The numerical code used to solve the Euler/Navier-Stokes equations (NSCODE) is developed at Polytechnique Montreal [79]. It solves the RANS equations on multiblock structured grids by using a second-order cell-centered finite volume discretization scheme. The time stepping is performed by using either an explicit multistage Runge-Kutta or an implicit Lower-Upper Symmetric Gauss-Seidel (LU-SGS) scheme [80]. The central differencing scheme can be stabilized by using artificial dissipation in the form of scalar [81] or matrix [82] dissipation. Also, the solution convergence to steady state is accelerated by the use of implicit residual smoothing, local time stepping, and a full multigrid scheme [83].

The 2D solver has been extended to solve the flow with a constant crossflow, which corresponds to the flow field around an infinite swept wing [84]. By imposing that all crossflow parameters are constant $\frac{\partial}{\partial y'} = 0$, the 3D equations become the same as 2D with the addition of the following convection-diffusion equation allowing to solve the transverse flow at every point:

$$\frac{\partial \rho v'}{\partial t} + u' \frac{\partial \rho v'}{\partial x'} + w' \frac{\partial \rho v'}{\partial z'} = \frac{\tau_{x'y'}}{\partial x'} + \frac{\tau_{y'z'}}{\partial z'} \tag{3.29}$$

This extension of the 2D solution allows the accurate calculation of aerodynamic features associated to swept wings with very little added complexity or computational time. In particular, the sweep angle affects i) the stagnation line at the leading edge, ii) the position and strength of oblique shocks, and iii) the separation point at the trailing edge and stall characteristics which are shown in Figure 3.6.

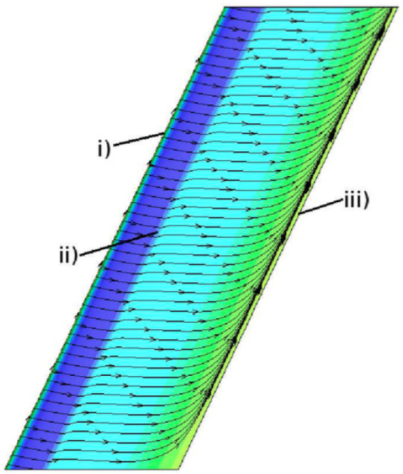

Figure 3.6 Surface streamlines on 20 deg infinite swept wing (source [6])

In the scope of this study, the 2.5D flow solutions are computed on the wing profiles and used to create a database that is then used to correct the Vortex-Lattice solution and obtain the finite wing loading including transonic and sweep angle effects.

Nonlinear Vortex Lattice Method

It is possible to apply a correction to the VLM solution to take into account viscosity and compressibility effects by changing the local angle of attack [27]. This correction can be based on experimental data or 2D RANS data and Gallay *et al.* [28] presented the use of 2.5D sectional RANS data to introduce the crossflow effects. This method has also been used by Parenteau *et al.* [7] for the optimization of the planform with combined low speed constraints arising from viscous effects and the stall margin of an aircraft and high speed constraints arising from compressibility effects at cruise speed. The correction is applied on the local angle of attack as proposed by Van Dam *et al.* [27] as opposed to a correction applied on the geometry, the so-called decambering approach [85]. Algorithm 3 illustrates how this correction is computed by comparing the theoretical lift coefficient slope of 2π and the actual slope as taken in the viscous database. The correction on the angle of attack is then iterated until converged, which means that the output force coefficient from the VLM matches that of the database.

Algorithm 3 Viscous correction

Solve the VLM system to compute $Cl_{inviscid}$
while $|Cl_{visc} - Cl_{inviscid}| < \epsilon$ **do**
  for every spanwise station i **do**
    Calculate the effective angle of attack :

$$\alpha_e(i) = \frac{Cl_{inviscid}(i)}{2\pi} - \alpha_{2D}(i) + \alpha_{3D} \tag{3.30}$$

    Interpolate the viscous lift in the database at the effective angle of attack:
$\alpha_e(i) \rightarrow Cl_{visc}(\alpha_e(i))$
    Calculate the angle of attack correction:
$\alpha_{2D}(i) = \alpha_{2D}(i) + \frac{Cl_{visc}(\alpha_e(i)) - Cl_{inviscid}(i)}{2\pi}$
  end for
  Compute forces for entire aerodynamic surface
end while

Figure 3.7 shows how the introduction of the viscous correction changes the VLM solution from one where the transverse flow is inexistent to one where it dominates the solution, especially outboard of the wing where a separation occurs, consistent with the fully 3D RANS data.

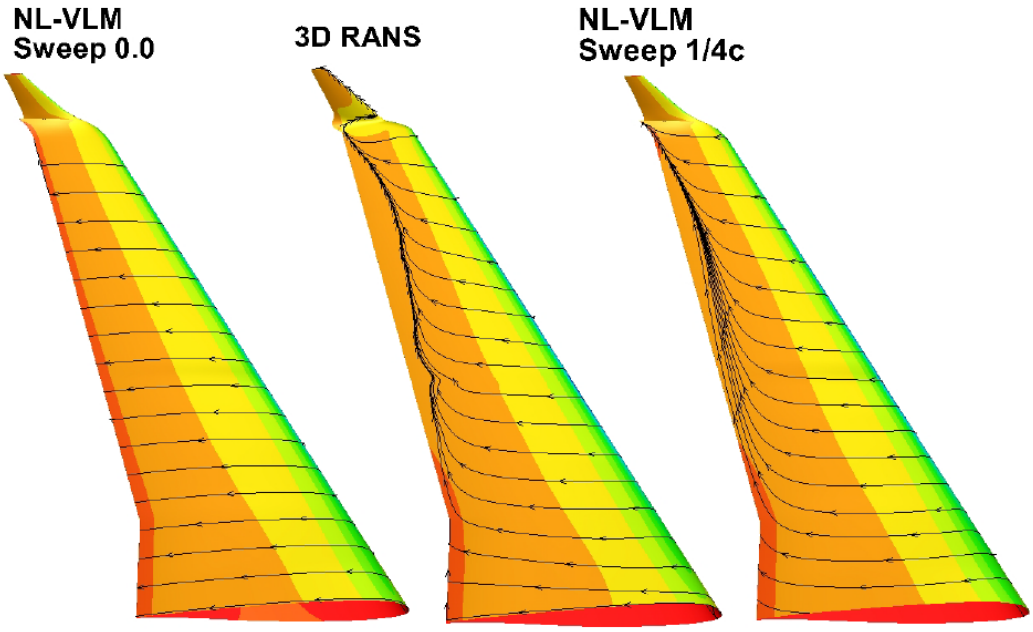

Figure 3.7 Comparison of surface friction lines on transonic swept wing showing the difference between no transerse flow (sweep = 0.0), transverse flow using the 1/4 chord sweep angle (sweep = 1/4c), and 3D RANS simulation (source [7])

It also allows the analysis of wings with partial span slats, flaps, and ailerons, as shown in figure 3.8, which makes this tool particularly useful for multi-topology aircraft wings where 3D meshing requires a significant investment of time and often consituted robustness issues. The VLM with 2.5D RANS correction approach, developed at Polytechnique Montreal, has been referred to as Nonlinear VLM (NL-VLM) for its ability to accurately capture nonlinear effects occuring at transonic speed as well as the C_{Lmax} at low speed and high angles of attack.

After the viscous coupling algorithm has converged, the lift is calculated by extracting the force coefficients from the database and applying the corresponding dimensional constants to obtain the physical units. This differs slightly from the standard VLM where the force would be computed at each panel and fully takes advantage of the RANS solver to integrate the pressure and shear-stress distribution on the airfoil.

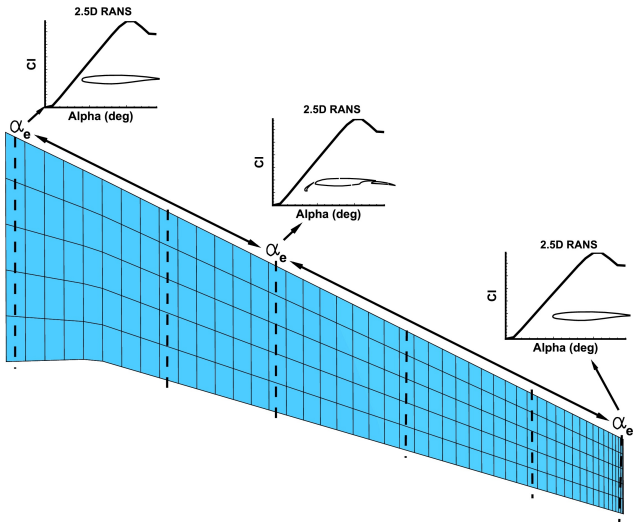

Figure 3.8 Viscous coupling along the planform with varying section

3.3 Static Aeroelastic Coupling

In order to couple the structural and aerodynamics solvers, the displacements and forces have to be interpolated and transferred from one mesh to the other. Because the vortex lattice grid is finer than the structural discretization, Farhat *et al.* [39] proposed that using the elements' shape functions ensures a conservative interpolation. Figure 3.9 illustrates this method, where a straight wing with its X-Y coordinate system and VLM grid is shown at the top and a linear two-node beam element below it. The forces are calculated at each streamwise row of panels using the 2.5D sectional RANS data and they are interpolated by using the shape functions N_1 and N_2 of the beam. The forces are then added at each nodes which constitutes the finite element model to resolve the displacements of the wing at each node.

The complete methodology can be summarized by algorithm 4. It can be seen that the overall loop is comprised of two main elements : NL-VLM and NL-FEM. In the first, a 2.5D RANS database is used in conjunction with a VLM tool to extract the forces on the planform including viscous, compressible and 3D effects. In the second, the deformation of the wing is calculated by using a nonlinear beam representation. Because the large deformations affect the shape of the planform, thus the aerodynamic loading must be recomputed and this also changes the deformed shape, this entire process must be iterated until the displacements and deformation energy of the wing are converged.

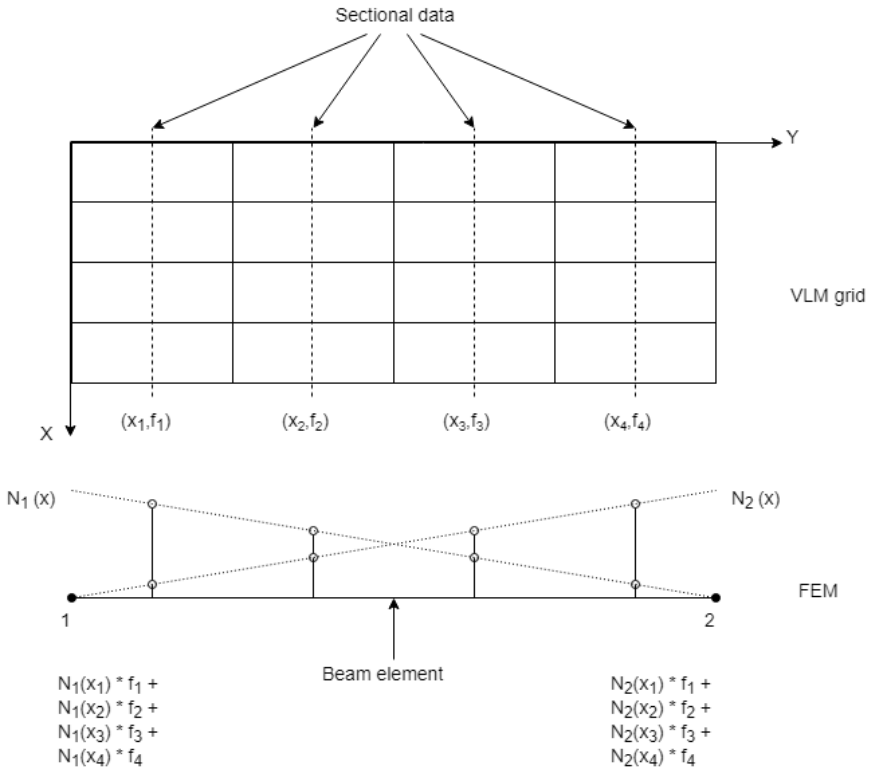

Figure 3.9 Interpolation of forces and displacements

Algorithm 4 Aeroelastic coupling

while $\mid E_i - E_{i-1} \mid > \epsilon$ or $\mid Cl_i - Cl_{i-1} \mid > \epsilon$ **do**
  Assemble the VLM system
  while $\mid Cl_{visc} - Cl_{invisc} \mid > \epsilon$ **do**
    for every spanwise station i **do**
      Solve viscous coupling
    end for
  end while
  for every spanwise station i **do**
    Compute and transfer the converged load to the nearest finite elements
  end for
  Assemble the finite element system
  while $\mid F - F_{int} \mid > \epsilon$ **do**
    Solve finite element model
  end while
  Displace the VLM planform with the converged displacements
end while

3.4 CAD Integration

A last problematic has emerged in the last few years, which concerns the accurate representation of the geometry in the different computational spaces. This is exemplified by the geometry representation workshop recently carried to study and tackle the challenges associated with this. In this study we use an approach strongly connected to the CAD by using strategies integrating a software developed at MIT by prof. Robert Haimes called Electronic Geometry Aircraft Design System (EGADS). The approach is inspired by the work of Kontogiannis *et al.* [86].

Figures 3.10(a) and 3.10(b) show a 2D mesh for an Euler computation using 64x64 elements on a NACA0012 airfoil. The mesh is quite coarse, but it is still important to recognize that discretizing the geometry to produce a mesh, even a fine one, already introduces discretization errors.

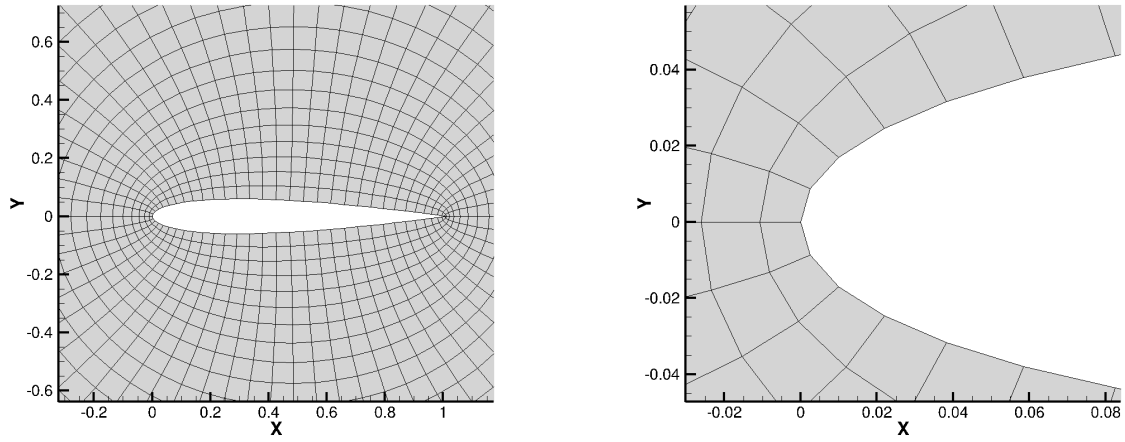

(a) (b)

Figure 3.10 2D Euler structured grids: a) airfoil and near field cells, b) discretization near the leading edge

In 3D, geometries are often simplified, for example by omitting slat supports and other structural details, which may present issues when performing comparisons with a complete aircraft during ground or flight tests. Figure 3.11 shows respectively the 3D geometry of an aircraft, the VLM representation of the wing, and the beam elements. This comparison highlights that careful interpolation between the non-matching interfaces is important.

In the present framework, a tool was created to enable the extraction of data directly from the 3D model through a python Application Programming Interface (API) and ESP. First,

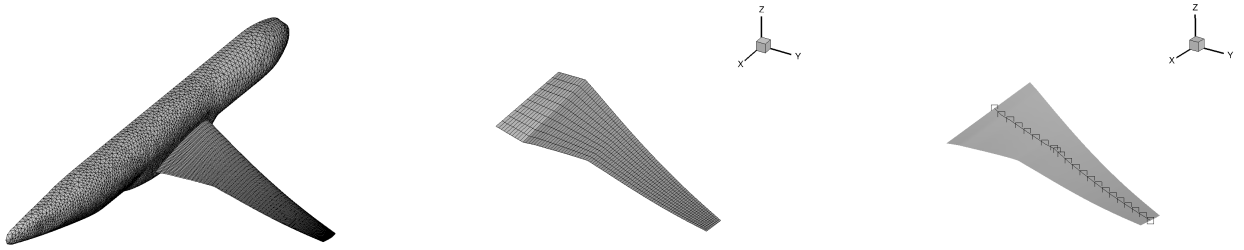

(a) (b) (c)

Figure 3.11 different representation of the NASA CRM: a) 3D geometry, b) VLM mesh, c) beam elements located at the shear center of the wing

the 3D computer model is read either in .stp, .igs or .egads format. Then, the intersection with the extraction plane is computed, the curves are discretized in a series of points that are then exported in a text file and the points are used to compute the sectional properties of the beams. The properties are computed by using the equations of Singer [87]. A top and side view of the NASA CRM wing 3D model is shown in figure 3.12 and the steps to extract the properties are illustrated in figure 3.13.

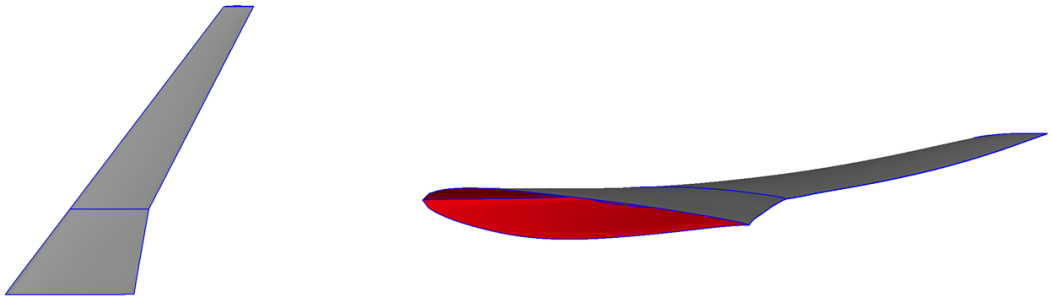

Figure 3.12 top and side view of the wing 3d model in EGADS

In addition to simplifying the extraction of sectional properties from a CAD file, this direct integration of CAD in the framework allows to maintain consistency between the different models and is especially useful in aeroelastic problems with non-matching interfaces.

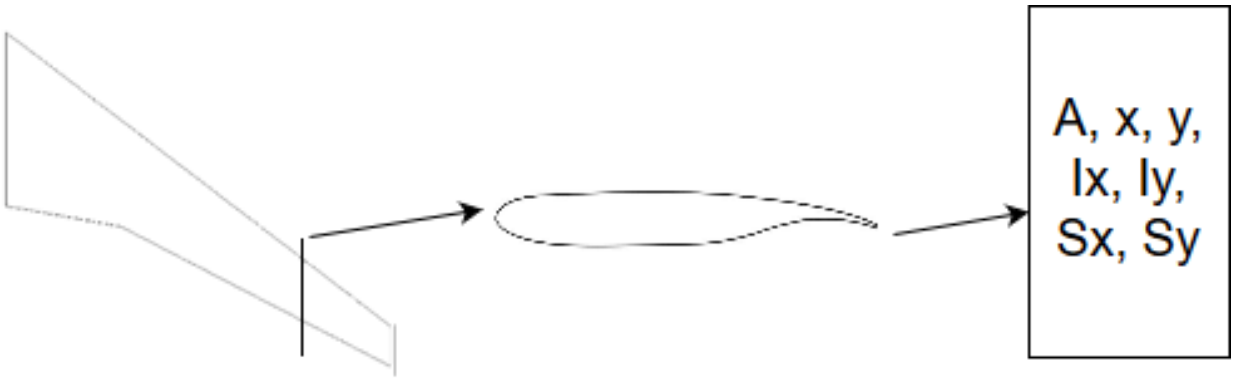

Figure 3.13 Schematic of properties computation

3.5 Conclusion

To summarize, the aeroelastic framework developed possesses the following characteristics that make it suitable for preliminary and conceptual design processes:

- Low computational cost and fast turnaround time;
- Nonlinear structural analysis based on beam elements;
- Nonlinear and medium fidelity aerodynamics analysis;
- Conservative interpolation of loads;
- Close integration of interfaces and geometry.

The following chapter will present some tests to verify the accuracy of the computation as well as validation cases for the framework.

CHAPTER 4 VERIFICATION AND VALIDATION

This chapter details verification and validation process of the aeroelastic framework. The implementation of the finite element analysis tool is first checked on linear and nonlinear cases before verifying the order of accuracy. Then, the aeroelastic test cases are introduced by first looking at a case of high-aspect ratio wing, then a case of control surface reversal, and finally an application on the NASA CRM, a transonic commercial aircraft.

4.1 Linear Resolution

The Finite Element Analysis tool is first tested with a linear cantilever beam with simple loading at the free end as illustrated on figure 4.1. The linear deflection of a beam when subject to a combination of forces can be obtained by the superposition principle as the addition of the deflection due to individual loads considered independently, which is not true for nonlinear analysis. The properties of the linear beam are listed in table 4.1.

Table 4.1 Properties for the linear beam

Quantity	Symbol	Units
Area	A	1 mm^2
Length	L	100 mm
Moment of inertia	I_y, I_z	10 mm^4
Polar moment of inertia	J	20 mm^4
Young's modulus	E	70e+3 MPa
Poisson ratio	ν	0.33
Force along x axis	P_x	100 N
Force along y axis	P_y	2 N
Force along z axis	P_z	1 N
Torsion	T	100 N mm

The analytical displacements (dx, dy, dz) and rotations (rx, ry, rz) can be calculated using Euler-Bernoulli beam theory and the properties listed above. The tension is calculated with the following equation :

$$d_x = \frac{P_x AL}{E} \tag{4.1}$$

The rotation of the beam due to torsion, where the shear modulus $G = E/(2(1+\nu))$:

$$r_x == \frac{TL}{GJ} \tag{4.2}$$

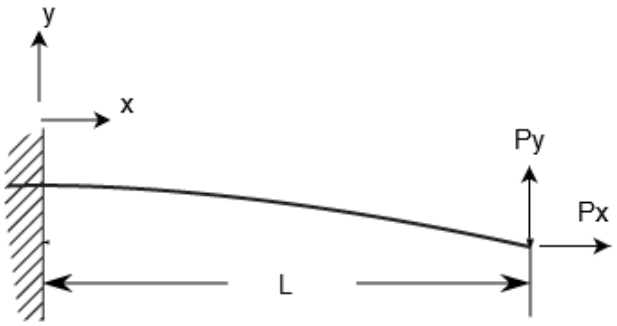

Figure 4.1 Linear beam with forces applied at free end

And the deflections and rotations due to bending :

$$d_y = \frac{P_y L^3}{3EI_z}, r_z = \frac{P_y L^2}{2EI_z} \tag{4.3}$$

$$d_z = \frac{P_z L^3}{3EI_y}, r_y = -\frac{P_z L^2}{2EI_y} \tag{4.4}$$

The analytical results are compared to the numerical solution in table 4.2 and it can be seen that the finite element analysis tool matches the theory for linear cantilever beams to a tolerance of 10^{-6} at least. This is expected as the load is applied at the end node of the beam, and this does not represent a case of distributed loading. Therefore, this verifies that the numerical implementation is good as it matches the analytical solution obtained by solving the differential equation.

Table 4.2 Solution for linear deflection of beam

	Analytical solution	Numerical solution
d_x (mm)	0.142857	0.142857
d_y (mm)	0.952381	0.952381
d_z (mm)	0.476190	0.476190
r_x (rad)	0.019	0.019
r_y (rad)	-0.007143	-0.007143
r_z (rad)	0.014286	0.014286

4.2 Nonlinear Resolution

The nonlinear algorithm is then tested on a case where a moment is applied at the tip and causes large rotations of the beam, shown in Figure 4.2. The parameters of the case are listed in Table 4.3. It can be seen in Table 4.4 and Figure 4.3 that the results of the nonlinear analysis compare well with that of NASTRAN sol 66 taken from Nastran nonlinear analysis user's guide [88].

Table 4.3 Properties of the beam with end moment loading

L	12 in
A	0.15 in^2
I_y, I_z	$2.813e^{-4}in^4$
E	$20e^6 lb/in^2$

Figure 4.2 Beam with moment applied at free end

Table 4.4 End moment nonlinear results

Moment (lb-in)	Nastran (deg)	OFEM (deg)
300	36.7	36.7
600	73.3	73.3
900	110.0	110.0
1200	146.7	146.7
1500	183.3	183.3
1800	220.0	220.0
2100	256.6	256.6
2400	293.3	293.3
2700	330.0	330.0
3000	366.6	366.6

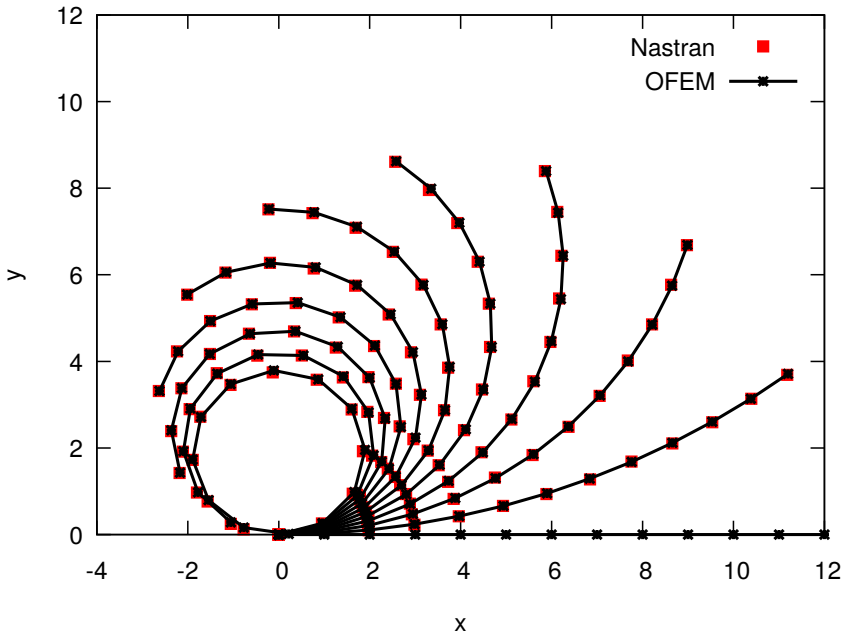

Figure 4.3 Nonlinear beam solutions

4.3 Order of Accuracy

In this section, the order of accuracy in space of the beam elements is presented to verify the implementation. The test case used is the same as that for the nonlinear deformation already discussed, a cantilever beam with a pure rotational moment applied at its end. The number of elements used is varied from 6 to 192 and these computations are repeated for several moments from 300 $in \cdot lb$ to 3000 $in \cdot lb$. Figure 4.5 shows the solution for the different number of elements when $M = 1800 in \cdot lb$.

It can be seen on figure 4.4 that the convergence rate of the solution is quadratic regardless of the load applied and the number of elements. This is explained by the fact that the linear beam formulation allows for quadratic resolution in space in the nonlinear resolution.

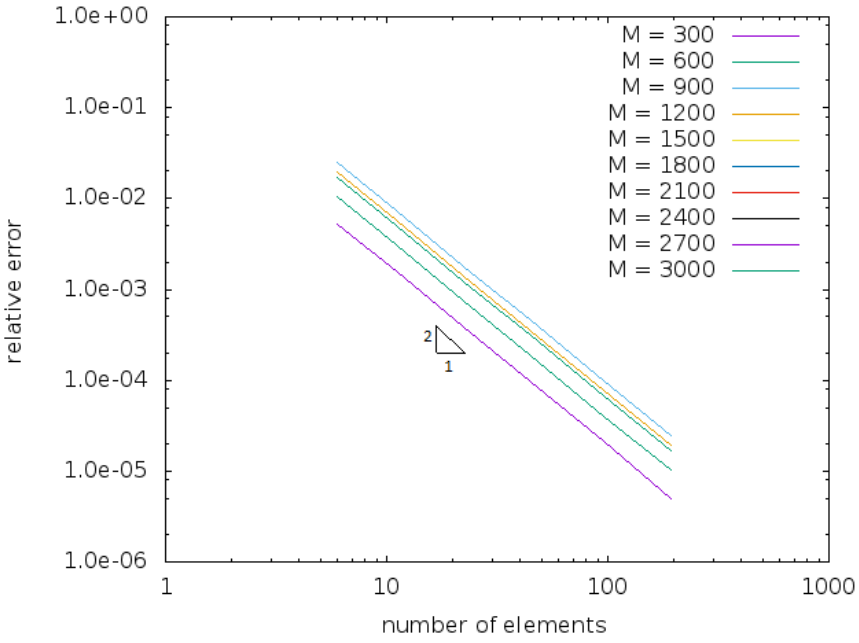

Figure 4.4 relative error of the numerical solution against the analytical solution for increasing mesh elements showing spatial convergence of beam elements

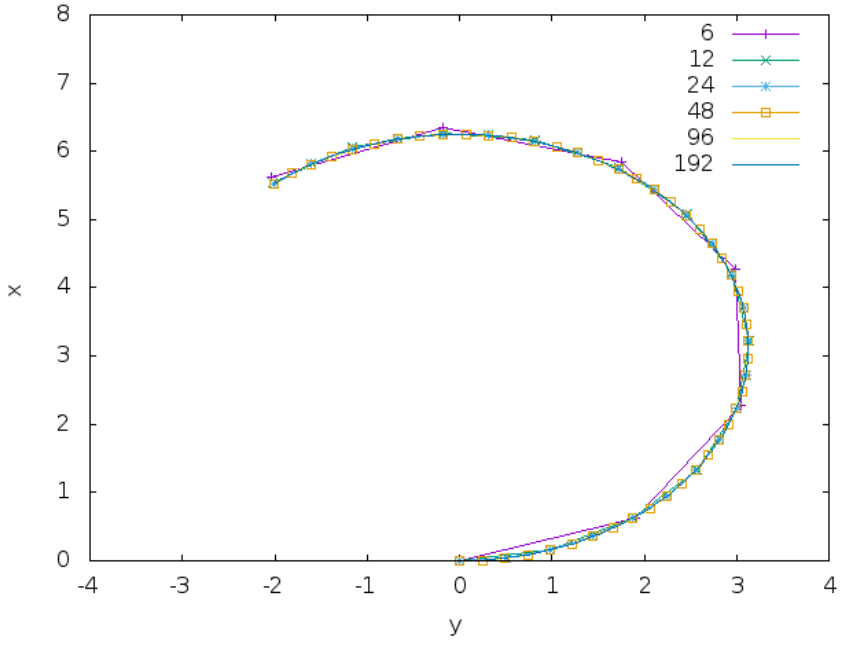

Figure 4.5 Solutions with various number of elements

4.4 High-Altitude Long-Endurance Aircraft

As it was seen in the literature review, High-Altitude Long-Endurance aircrafts are very present in the recent scientific publications. Various reasons can explain this surge in interest: first, the geometry is simple from an aerodynamics and structural mechanics standpoint; second, the flight conditions are not very challenging, allowing the focus to be on other physical phenomena and interactions; third, static aeroelastic phenomena dominate the steady flight characteristics of these vehicles, therefore converting commercial interests in these configurations into scientific interest on the challenges.

The computations performed in this section aim at validating the aeroelastic framework, especially the coupling methodology for large static deflections of the planform. The case is the same as that studied by Smith *et al.* [42] and Murua *et al.* [43], thus the results are compared to those two references and differences in methods and their impacts are detailed.

In this section, the convergence and energy conservation of the coupling method are highlighted while comparing the aeroelastic deformation of a high-aspect ratio wing shown in Figure 4.6. The conditions of flight are an altitude of 20 000 m, a velocity of 25 m/s. The structure is represented by a beam located at 50% chord and has the properties listed in table 4.5.

Table 4.5 Properties for the high-aspect ratio wing

Quantity	**Symbol**	**Units**
Half Span	b	16 m
Chord	c	1 m
Flexural rigidity	EI	$2.0e^4$ Nm^2
Torsional rigidity	GJ	$1.0e^4$ Nm^2

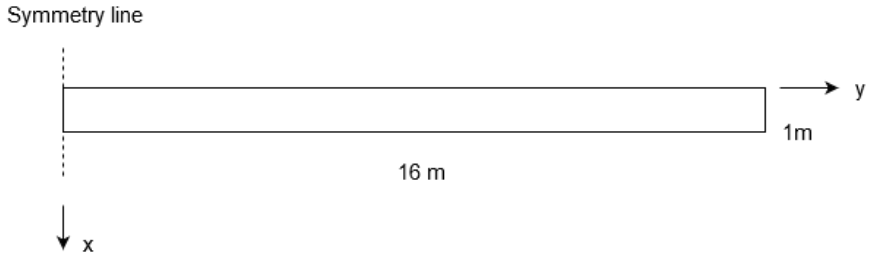

Figure 4.6 High-aspect ratio wing planform

The aeroelastic simulation is solved at an angle of attack (α) of 2 and 4 degrees and it takes approximately 12 iterations to reduce the numerical error by 6 orders of magnitude on the

lift coefficient as well as the deformation energy. Furthermore, at each aeroelastic iteration, the structure's residual dropped to 10^{-6} as well within 6 Newton iterations.Figure 4.7 shows the error between subsequent structural iterations, which is the norm of the ΔD vector representing the change in position of all degrees of freedom. Also, Figure 4.8 shows that the lift coefficient and total potential energy and it can be seen that both behave similarly, with a slight overshoot.

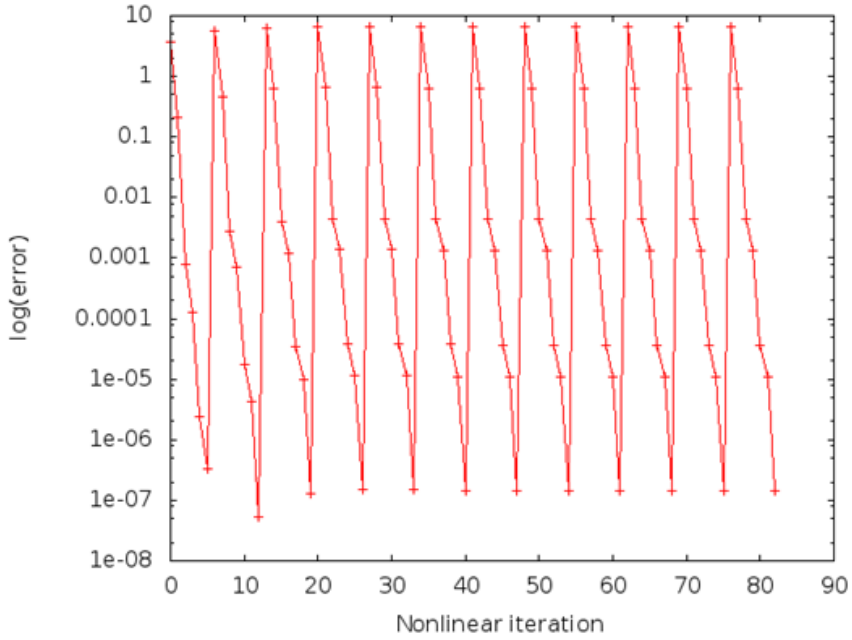

Figure 4.7 Convergence of the finite element algorithm for the entire aeroelastic analysis

The results for the high-aspect ratio wing are compared to those of Smith *et al.* [42] who used a nonlinear beam model to represent the structure of high-aspect ratio wings and showed that this representation is superior to the linear theory, especially at higher angles of attack because the large deflections unphysically stretch the planform. The deflections results are also compared to those of Murua *et al.* [43], who used a nonlinear beam model and vortex lattice method as well.

Furthermore, the results shown in Figures 4.9 and 4.10 are obtained with different aerodynamic models. Smith *et al.* [42] use an Euler computational fluid dynamics solver whereas the present framework uses potential VLM, without vortex corrections applied. It is expected that in low speed high-altitude flight regime used in this study, the Euler equations and potential equations should give close results and this claim is verified in subsection 4.4.2.

It is important to note that the convergence threshold stated by [42] is 2%, while in this study a maximal error of $1.0e-6$ is used as a numerical convergence criterion.

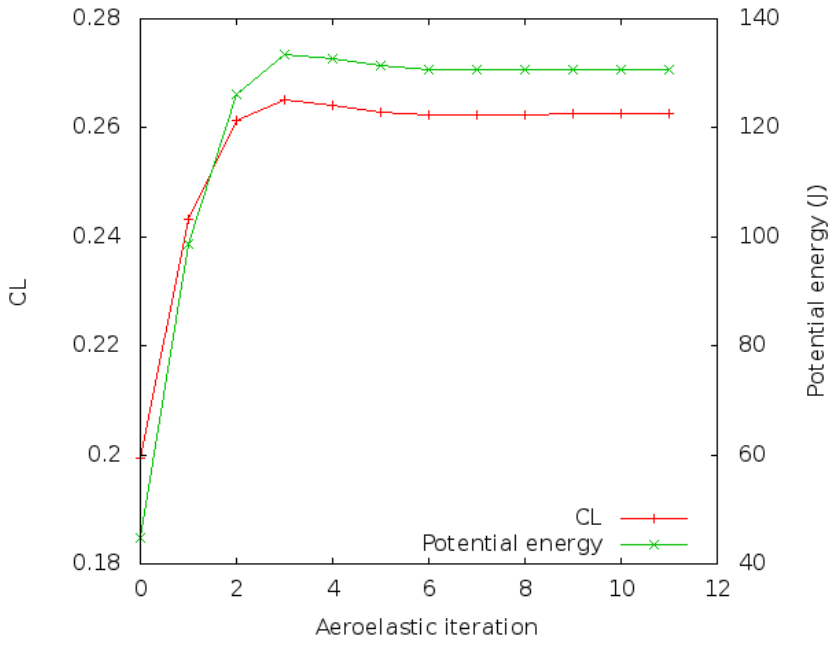

Figure 4.8 Convergence of lift coefficient and elastic potential energy in the structure

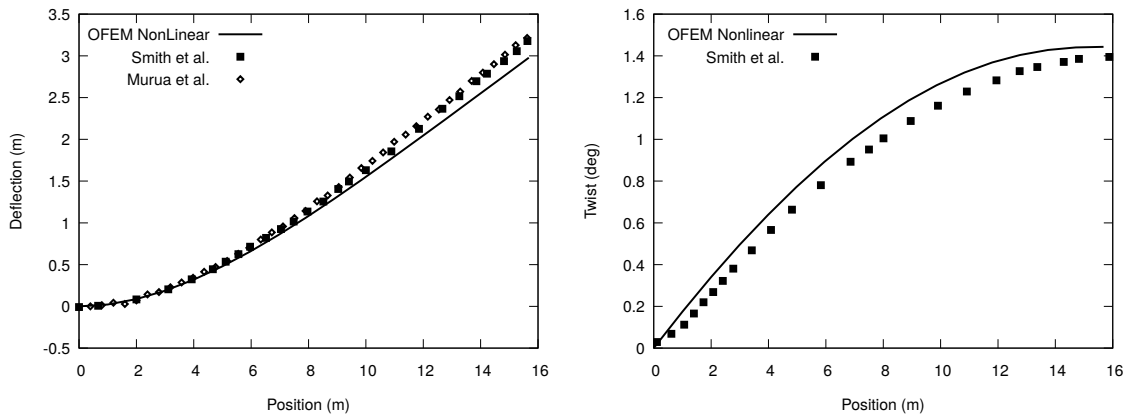

(a) (b)

Figure 4.9 Deflection and twist at 25 m/s and α 2 deg

4.4.1 Refinement study

To further verify our results, comparisons between the results obtained for various VLM discretizations are performed. The number of panels chordwise was varied from 10 to 40 by a multiplication factor of 2, and the spanwise number was changed from 100 to 200. Figures 4.11 through 4.12 show the deflection and twist of the planform for the various mesh refinements. These results show that the spanwise number of panels has almost no effects

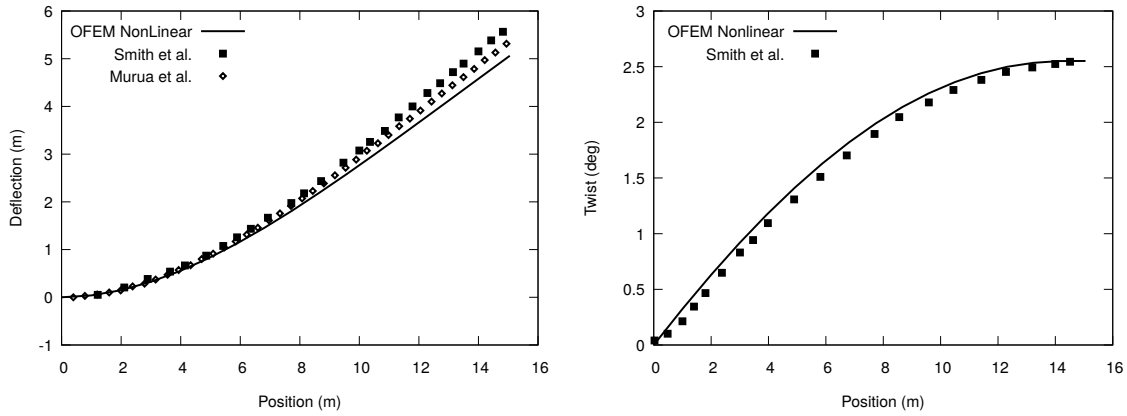

(a) (b)

Figure 4.10 Deflection and twist at 25 m/s and α 4 deg

on the loading of the wing as both simulations are indistinguishable on both graphs for a number of elements higher than 100. On the other hand, the chordwise discretization has an important effect on the pitching moment, where it seems that using fewer panels overpredicts the twist of the wing. The same process is repeated for the number of spanwise panels in figures 4.13 to 4.14 and it is possible to conclude that a discretization of ≈ 100 panels spanwise is sufficient to correctly represent the wing loading.

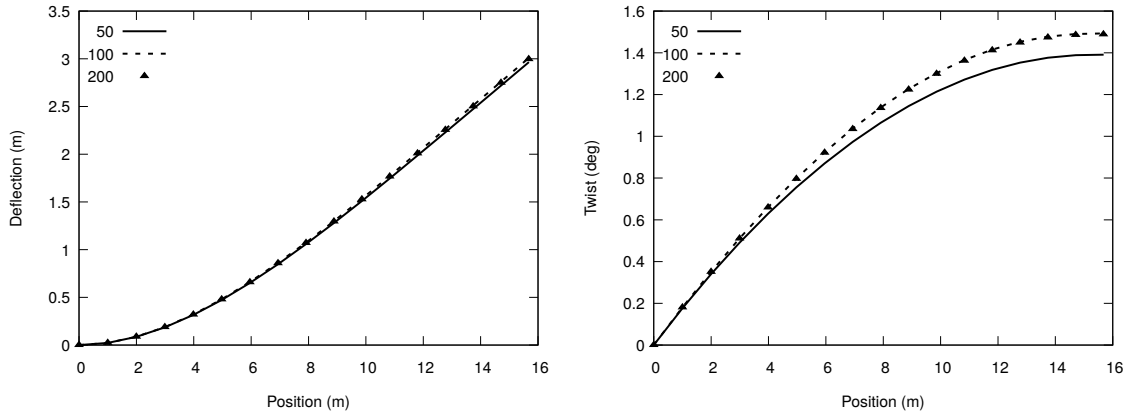

(a) (b)

Figure 4.11 Deflection and twist of the wing at $\alpha = 2.0$ deg. for different mesh refinements spanwise

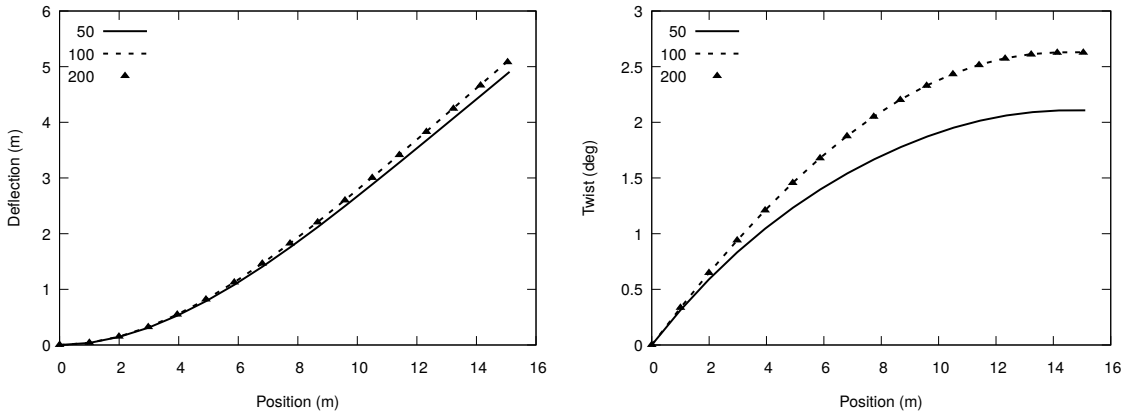

(a) (b)

Figure 4.12 Deflection and twist of the wing at $\alpha = 4.0$ deg. for different mesh refinements spanwise

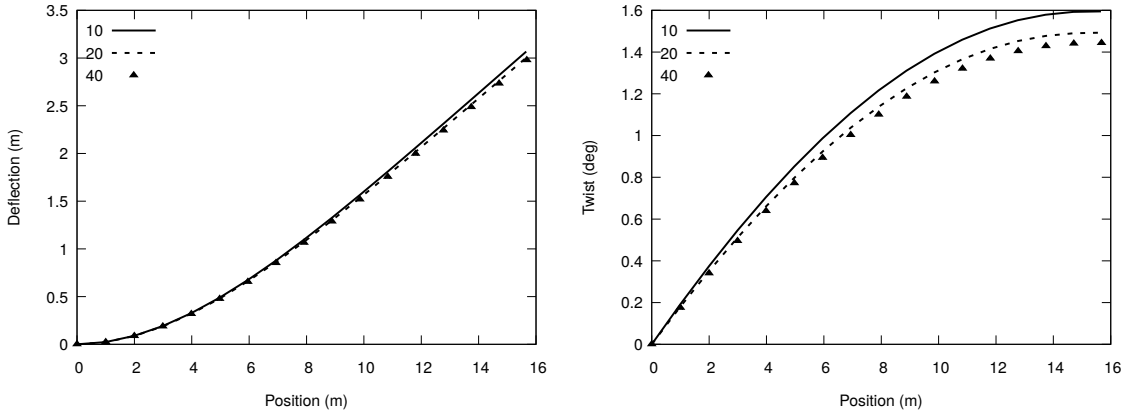

(a) (b)

Figure 4.13 Deflection and twist of the wing at $\alpha = 2.0$ deg. for different mesh refinements chordwise

4.4.2 Viscous coupling algorithm

To make sure that the viscous coupling algorithm performs as expected, the numerical computations are repeated with the use of the viscous database for a NACA0012 airfoil. The aerodynamics loads are similar between the thin airfoil theory and the RANS computations on a symmetrical airfoil. In particular, the lift coefficient is close at the same angle of attack, but the symmetrical airfoil will exhibit a small pitching moment that the thin airfoil theory does not predict. Therefore, it is expected that the two computations will start to diverge as the angle of attack increases. The aeroelastic deflections computed with and without viscous

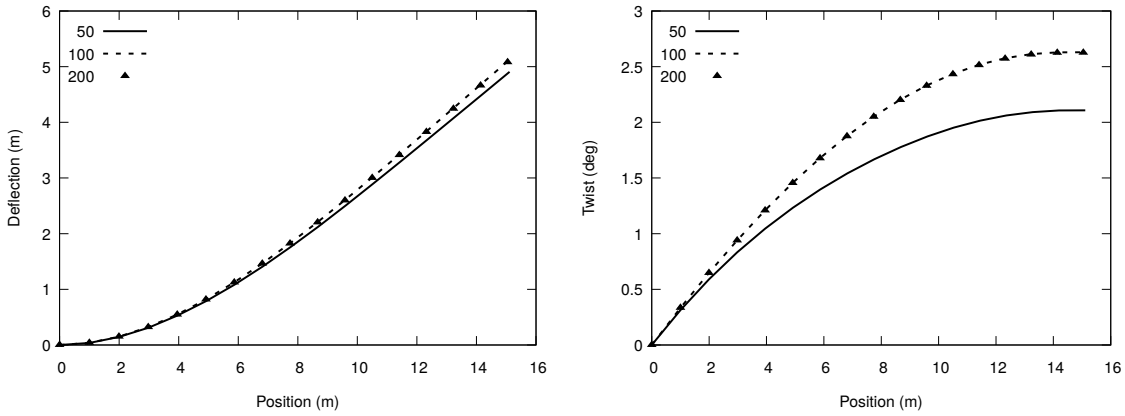

(a) (b)

Figure 4.14 Deflection and twist of the wing at $\alpha = 4.0$ deg. for different mesh refinements spanwise

coupling are compared on Figures 4.15 and 4.16.

As predicted, the deflections match well, but there are discrepancies in the twist, reaching 0.5 deg in the $\alpha = 4.0$ deg case, but these are believed to be attributed to the differences between the inviscid VLM and the pitching moment present in the RANS database. An important note is that the use of the viscous correction approach in the computation of the aerodynamic loading removes the dependency of the solution on the chordwise discretization. This is attributed to the fact that the coupling algorithm converges the strength of the vortices to correspond to the values of the database, but the pitching moment is taken directly from the interpolated value at the correct effective angle of attack.

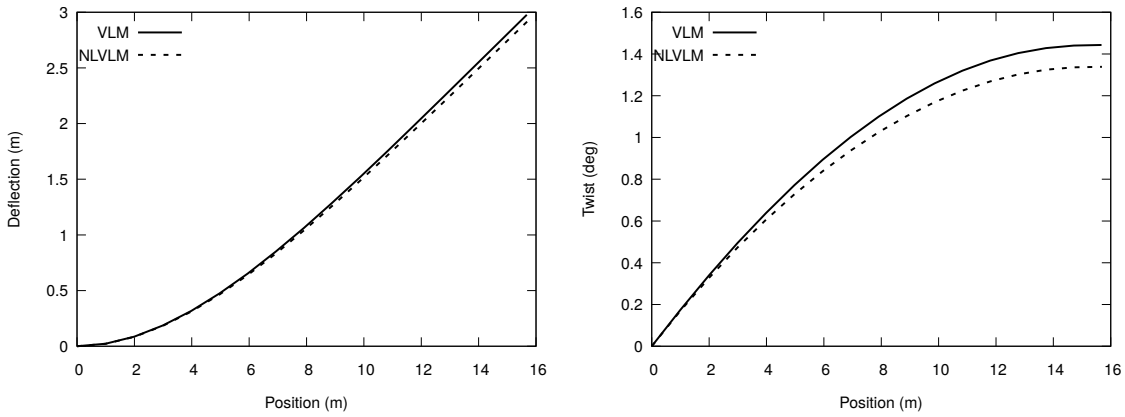

(a) (b)

Figure 4.15 Deflection and twist of the wing at $\alpha = 2.0$ deg. for VLM and NLVLM

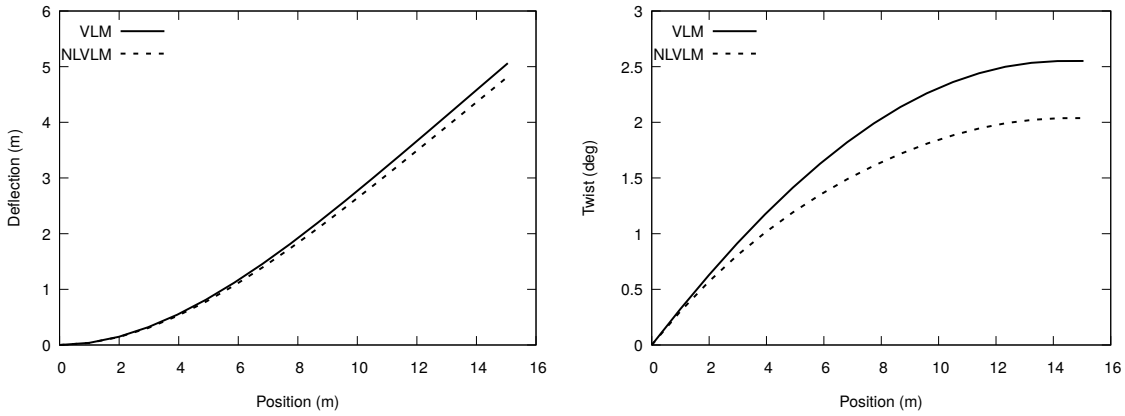

(a) (b)

Figure 4.16 Deflection and twist of the wing at $\alpha = 4.0$ deg. for VLM and NLVLM

4.5 Aileron Reversal

This test case is an application of the framework to transonic and supersonic flight conditions. This is, in a sense, the opposite of the HALE problem, where aeroelastic phenomena are driven not from the flexible structure, but rather from the changes in aerodynamic loads at various flight velocities. The case is from Andersen *et al.* [63], later expanded with viscous effects by Eastep *et al.* [64] and the wing used is a modified Goland Wing shown in figure 4.17.

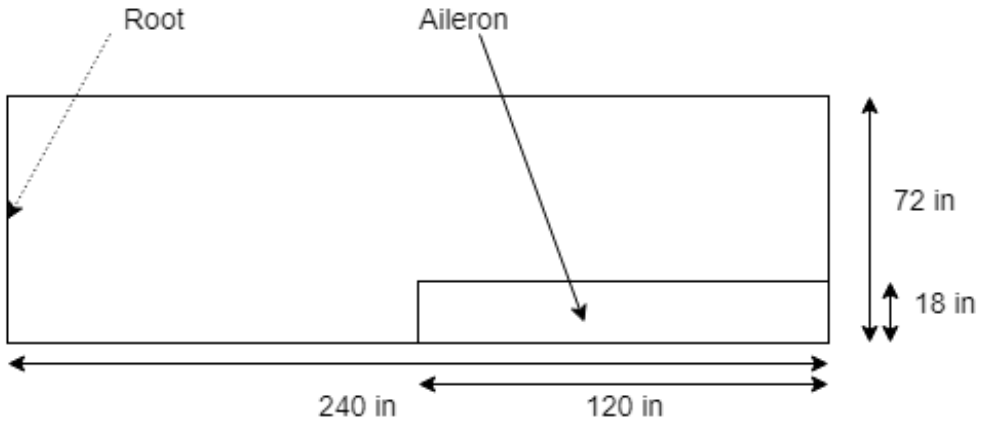

Figure 4.17 Planform of transonic wing

The mesh used for the viscous database is generated for the parabolic airfoil with and without flap. The mesh used is an O-mesh with 513x385 cells for the RANS simulations and 257x257

for the Euler simulations shown in figure 4.19. Both RANS and Euler equations are used to allow the assessment of viscous effects on the reversal speed, and the Spalart-Almaras turbulence model is used along with the implicit LUSGS solving scheme.

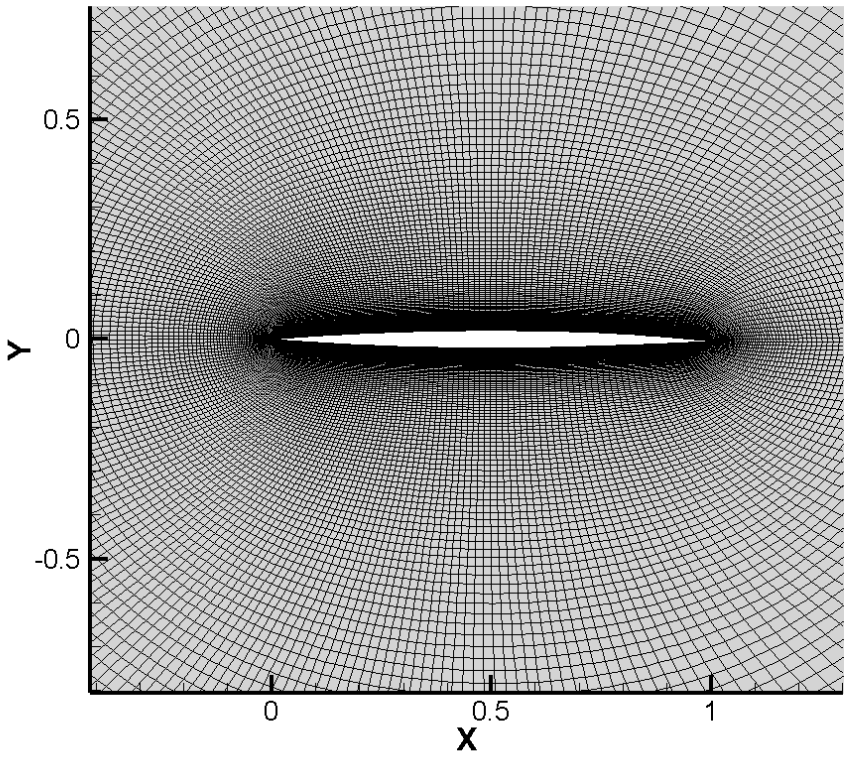

Figure 4.18 Mesh used for the RANS solutions

The effect of the viscous terms on the Cp distribution is shown in Figure 4.20. It is evident that the overall resultant forces are different, which outlines what was said in the literature review: Euler simulations are not as physically accurate as RANS because of their tendency to resolve the shock position and strength incorrectly. In this particular case, the pressure difference is much more concentrated aft of the airfoil and this results in a higher pitching moment at the same angle of attack.

The effect of the control surface deflection on the Cp distribution with RANS solver is shown in Figure 4.21. It is intuitive that deflecting the aileron will increase the resulting lift for a symmetrical airfoil, but this image also shows that there is a slight shift towards the trailing edge in the position of the center of pressure. This is seen because the two curves are not only offset vertically, but the two parts of the hinged solution are also shifted horizontally.

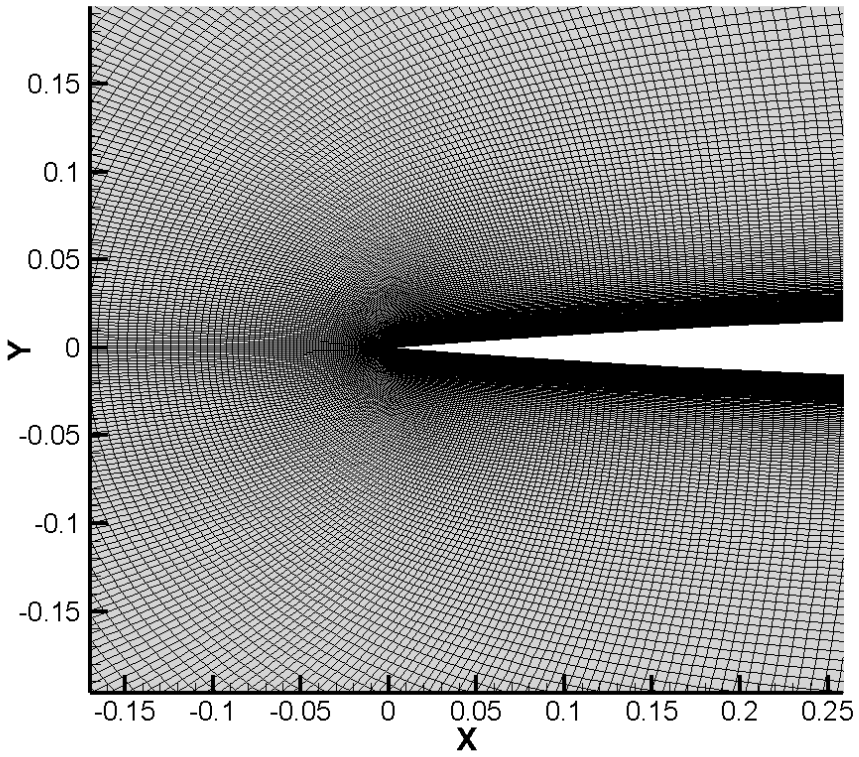

Figure 4.19 Mesh used for the RANS solutions around the tip of the airfoil

The pressure contours around the airfoil are shown in Figure 4.22 where the position and strength of the shock clearly differs between the two aerodynamic models.

The rolling moment coefficient is calculated by using Eq. (4.5) for the rigid planform at different mach numbers. This equation involves integrating all rigid aerodynamic forces and their resulting moment around the x axis along the planform. The results and compared with those from Eastep *et al.* [64] in figure 4.23.

$$C_M = \frac{M_x}{q\ S\ b} \tag{4.5}$$

The moment coefficient comparison highlights that the rigid forces match the TSD results in trends. For example, the highest rigid rolling moment is reached at a similar Mach number of 0.9. On the other hand, the values are higher for the NL-VLM at all values below $M = 0.9$ by a factor of almost 2. The Euler and RANS results are closer to the Nonlinear TSD than the linear TSD, for which the peak occurs at the sonic point. Consistent with the previous

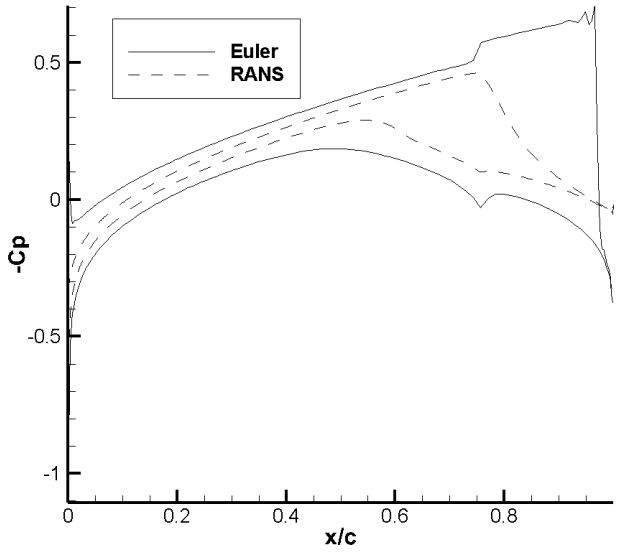

Figure 4.20 Comparison of Euler and RANS Cp distribution at Mach 0.90, $\alpha = 0.0$ deg, Re = 39.4e6, flap deflected

discussion, the forces applied on the wing with the RANS model are considerably less than for the Euler equations. Especially in the case of a rigid wing, these results point toward differences in the aerodynamic models, namely a higher lift coefficient for the parabolic airfoil when computed by the RANS and Euler equations over the TSD model.

The control-surface effectiveness is calculated at different dynamic pressure values for the same Mach number. The effectiveness of the control surface is defined by Eq. (4.6).

$$\epsilon = \frac{C_{M_{\delta\alpha,flexible}}}{C_{M_{\delta\alpha,rigid}}} \tag{4.6}$$

where the rigid moment coefficient is the one shown previously, while the flexible moment coefficient is the non-dimensionalized rolling moment with the forces computed in the final, converged deformed state of the wing.

The process outlined above is repeated for several Mach numbers and the dynamic pressure at which the effectiveness drops to 0 is extracted, which corresponds to the reversal pressure (q_{rev}). This is plotted in figure 4.24. Effectively, this is the point at which the deflection of the flap on the wing incurs no change in the balance of forces on the aircraft, which can be detrimental to the flight.

The overall trends of all the curves are the same, where the pressure at which reversal occurs dips as Mach number approaches one and increases afterwards. The RANS, Euler, and

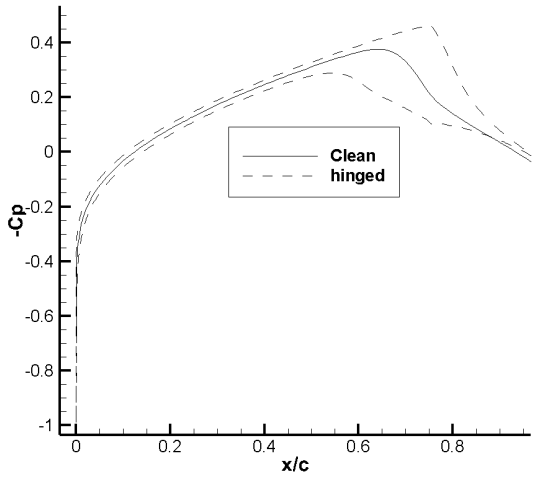

Figure 4.21 Cp distribution at Mach 0.90, $\alpha = 0.0$ deg, Re = 39.4e6

nonlinear TSD curves reach their lowest reversal pressure at $M = 0.92$, where the linear model is at its lowest at $M = 1.0$. The pressures obtained by the NL-VLM model are considerably lower, on the order of 20%. This is probably linked to the difference in rolling moment that was observed for the rigid solutions.

In order to verify the aerodynamic computations performed to construct the 2.5D RANS and Euler database, a comparison is done with an Open-source CFD solver. This solver is named *SU2* and an entirely new mesh, using the same resolution, was generated by using the commercial mesher *Pointwise*. The same solver parameters were used, except that *SU2* uses a GMRES implicit solver. Figure 4.25 shows the comparisons between the Euler solutions for both the in-house and the open-source code.

The comparison shows that the database results match closely the results obtained independently by another software. It is therefore likely that the discrepancies between the results for the rolling moment and the reversal pressure, when compared to the reference, emerge from the difference between the different approaches for computing the aerodynamic solutions. A more extensive comparison between RANS and TSD should be done to pinpoint the source of the difference. It is also possible that the structural models used between the two codes were ultimately different, producing different aeroelastic solutions. This is less likely because both models are reported to be stick models, and the parameters of the beams are explicitly stated and constant for the entire wing.

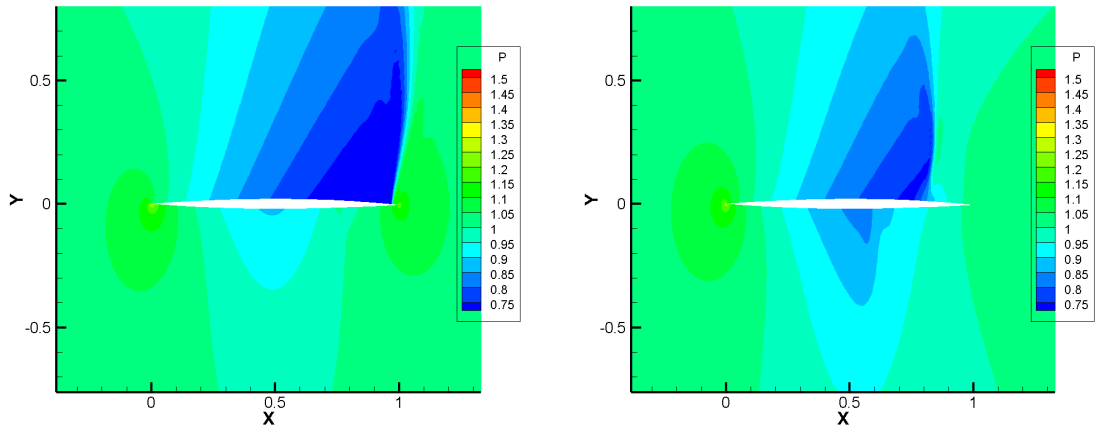

(a) (b)

Figure 4.22 Pressure contours for a) Euler and b) RANS simulations on the parabolic airfoil

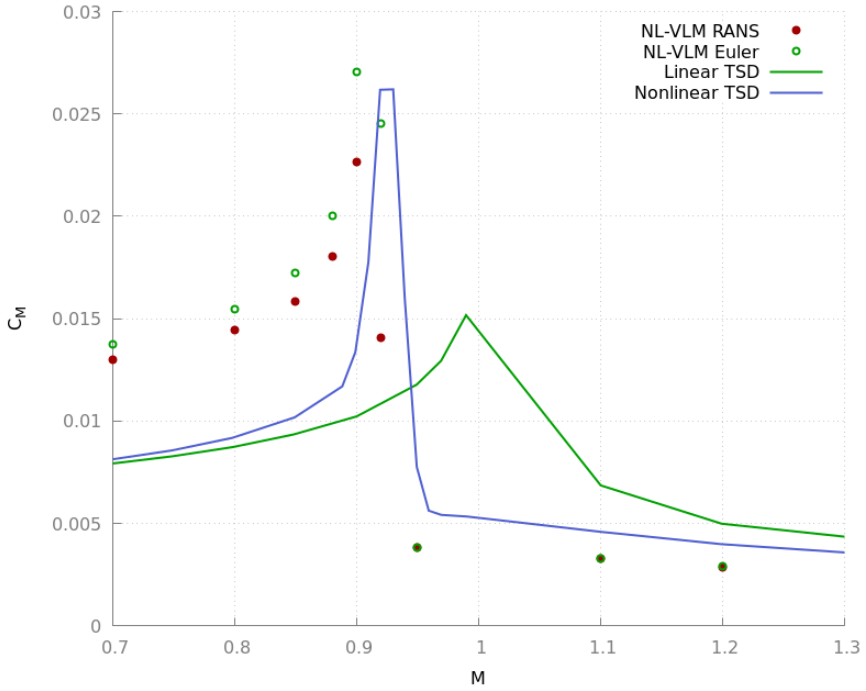

Figure 4.23 Variation of rigid rolling moment coefficient with mach number

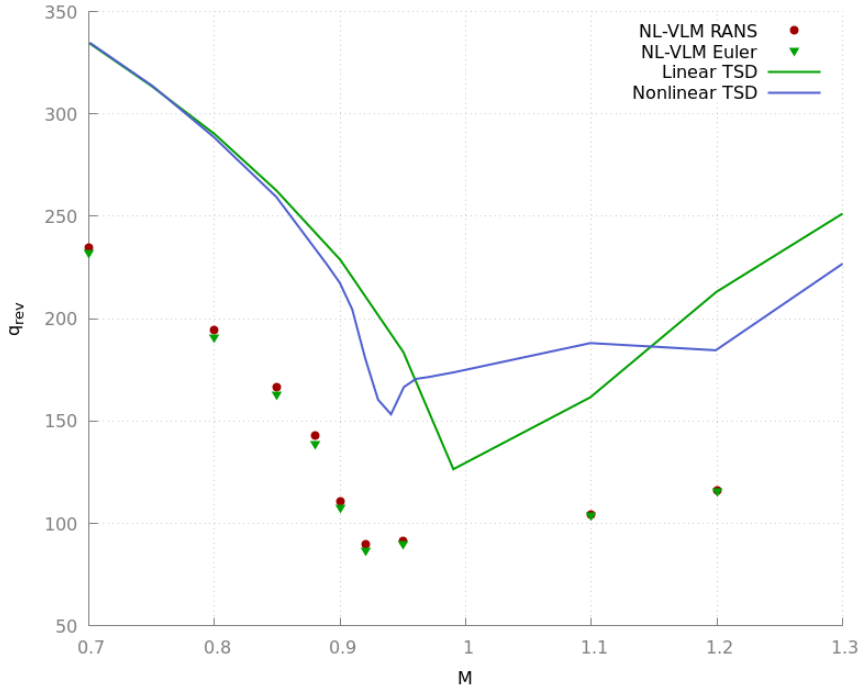

Figure 4.24 Variation of the reversal dynamic pressure with Mach Number

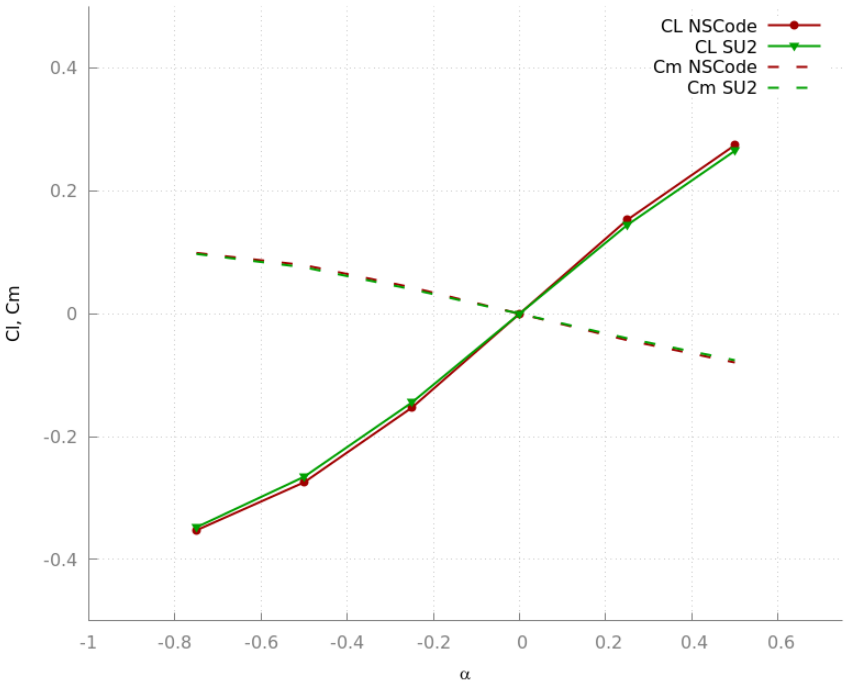

Figure 4.25 Lift and pitching moment coefficients for the parabolic airfoil at $M = 0.9$

4.6 NASA Common Research Model

The Common research Model (CRM) was developed by Vassberg *et al.* [89] to act as a representative baseline model for the validation of CFD methods. It consists of a typical transonic commercial aircraft design, with swept wing and supercritical airfoil section. Its popularity has extended beyond purely aerodynamic validation studies to shape, weight, and structural optimisation as well as aeroelastic phenomena. To this effect, NASA performed experimental tests on an aeroelastic windtunnel model at the European Transonic Windtunnel (ETW) in 2017. This acronym is used in the following figures to refer to the experimental results obtained during this test campaign.

The validation shown in this section consists of comparing the deflection and twist of the wing obtained with the current framework against the results of other authors that used different high-fidelity methods. This is done to evaluate the application of the tools developed in an industry relevant case for conceptual and preliminary design. The CRM wind tunnel model has the parameters shown in table 4.6. More information is available on the webpage dedicated to the NASA CRM (https://commonresearchmodel.larc.nasa.gov/).

Table 4.6 Simulation parameters for the CRM aeroelastic study

Parameter	**Value**	**Units**
Aspect ratio (AR)	9.0	-
Wing span	0.7934	m
Taper ratio (λ)	0.275	-
Mean aerodynamic chord (m.a.c)	0.18923	m
Reference Area	0.2796	m^2
Leading edge sweep angle	35.0	deg.
Mach number	0.85	-
Atmospheric pressure	191.0	KPa
Temperature	300.0	K

Figure 4.26 shows the top view of the planform and the corresponding VLM discretization. The VLM discretization in this case consisted of 150x10 panels, but the chordwise number of panels did not affect the final solution as the viscous coupling was used. A refinement study similar to the one done on the HALE aircraft was performed to verify this. Also, the fuselage was neglected because the VLM is not able to accurately represent a closed body that is connected to a lifting surface. On the other hand, the fuselage effects on the lift distribution are mostly concentrated inboard, where the wing structure is large and stiff. Therefore, even though this constitutes a significant simplification, it is unlikely to produce large discrepancies between the physical model and the numerical simulation.

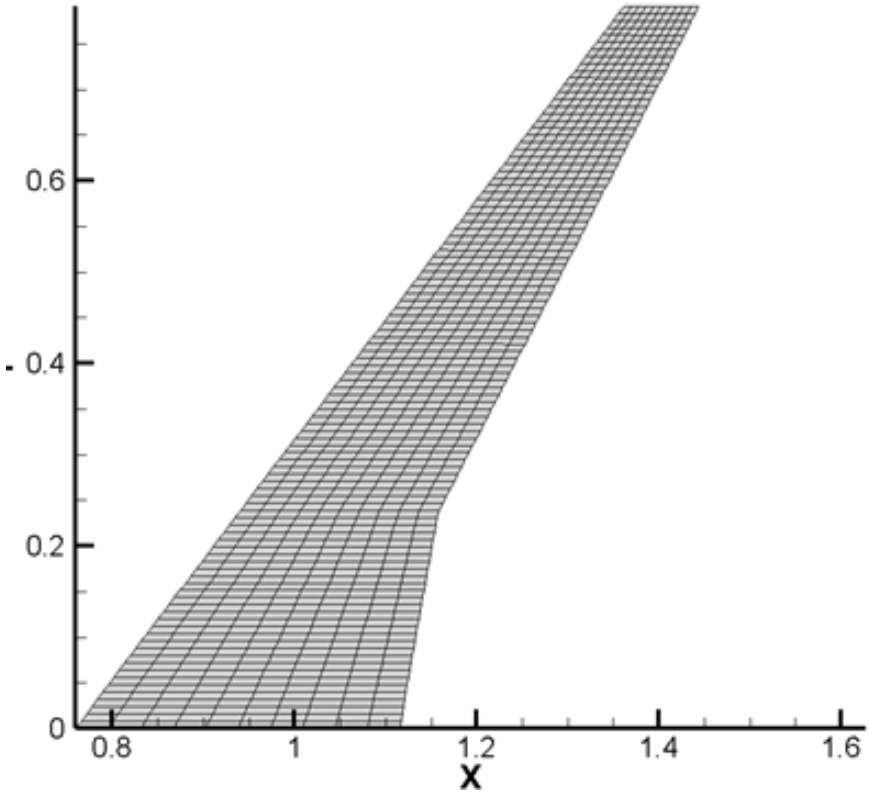

Figure 4.26 Top view of the CRM wing and VLM discretization

The viscous database is also generated by using the in-house 2.5D RANS solver. The properties of the beam elements were also extracted automatically from cuts of the CAD model.

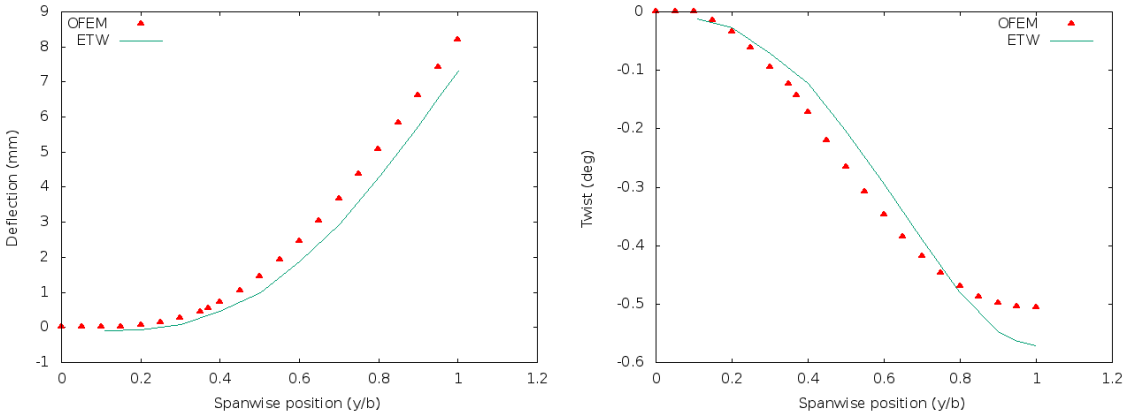

(a) (b)

Figure 4.27 Deflection and twist of the wing at $\alpha = 1.0$ deg.

The results can be seen to match very well with the experiments and they compare nicely

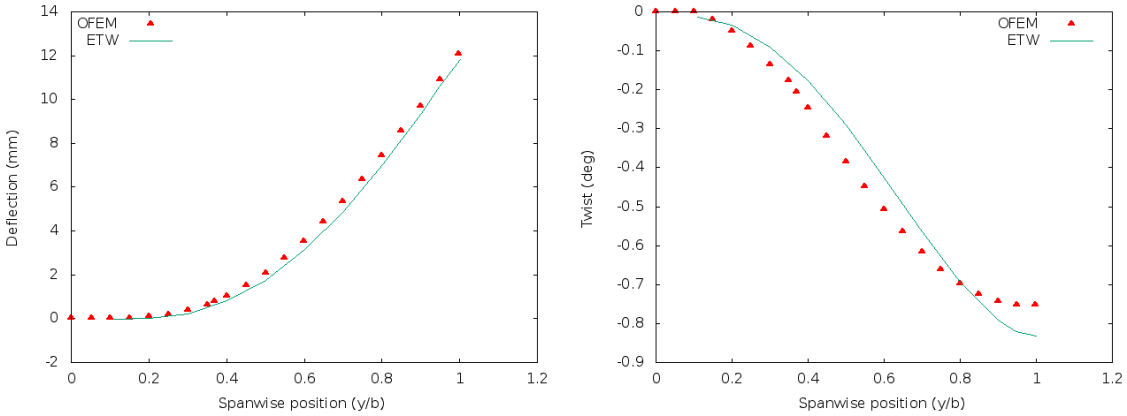

(a) (b)

Figure 4.28 Deflection and twist of the wing at $\alpha = 2.0$ deg.

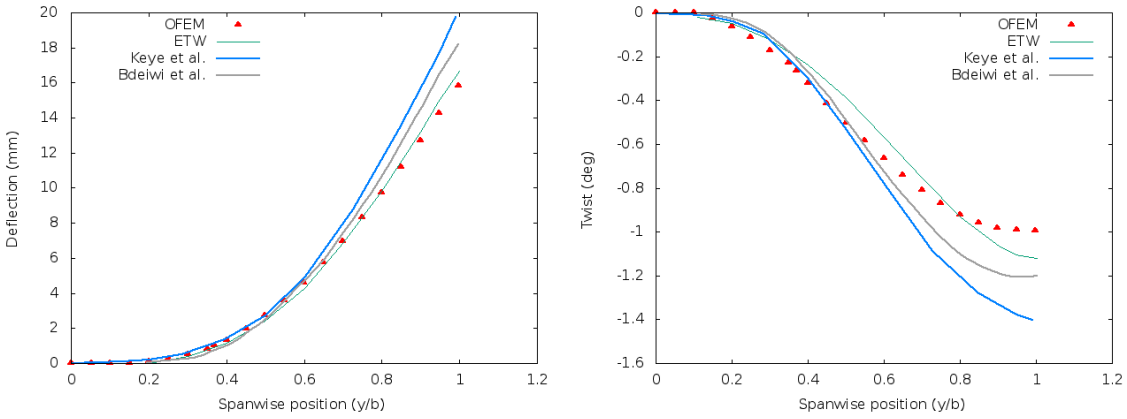

(a) (b)

Figure 4.29 Deflection and twist of the wing at $\alpha = 3.0$ deg.

with the other studies performed on the subject, even though higher fidelity models were used. At all angles of attack, the deflections are well represented by the VLM model while the twist has small discrepancies at the tip.

For the cases $\alpha = 3.0$ and 4.0, it can be seen that the results of Bdeiwi *et al.* [32] are close to the experiment, but the error is larger than with the present framework. Results by Keye *et al.* diverge even more from the experiment. This is surprising considering that the lower fidelity method performs best. This is probably not a general case, as more validation could produce results where assumptions made in the present framework change the solution significantly. An example of this is a case where the engines and nacelles affect the aerodynamic solution. On the other hand, the objective of this research was to produce a framework suitable for the

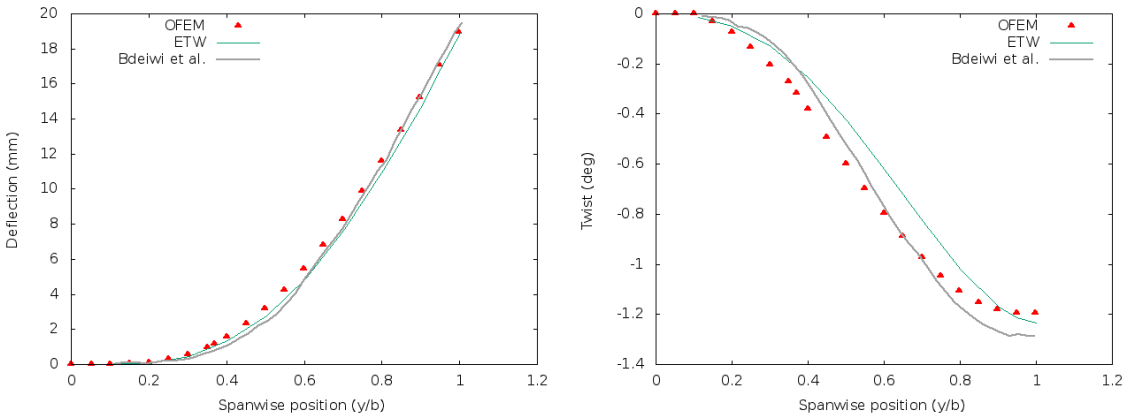

(a) (b)

Figure 4.30 Deflection and twist of the wing at $\alpha = 4.0$ deg.

preliminary and conceptual design of aircrafts, where such hypotheses are often reasonable and where higher fidelity methods are not practical.

4.7 Conclusion

This section has shown the verification and validation of the developed framework by comparing the results with analytical, numerical, and experimental results from various sources. The structural solver is accurate and consistent with the underlying theory.

The first application, the HALE aircraft, provided a simple testing ground for the method as it lies fully in the application range of the VLM, providing good insight into the performance of the coupling methodology. The results were shown to be in good agreement with those obtained with similar aerodynamic and structural models. Also, the refinement study and comparison between inviscid and coupled VLM showed that the results were fairly insensitive to changes in the way the problem is numerically constructed, although the number of chordwise panels had a stronger influence on the twist of the wing.

The second application is the aileron reversal. This case is a test on the extent to which the viscous correction enables the accurate prediction of the aeroelastic behavior of the wing in the transonic and supersonic range. The solver is able to correctly predict control effectiveness trends, but the results, when compared with the transonic small disturbance aerodynamic model, are not exactly the same. Very few studies exist on this particular problem, therefore it could be interesting to compare the results with a 3D RANS aeroelastic computation.

The last application is the CRM, for which the deflection and twist of the wing in cruise

conditions are presented. Overall, the results closely match the experimental results. Further, in some instances, the current methodology seems to outperform high fidelity models. This is surprising considering the enormous difference in computational time between both VLM (10^3 dofs) and 3D RANS (10^7 dofs) as well as a beam model (10^2 dofs) and a 3D finite element model (10^6 dofs).

CHAPTER 5 CONCLUSION

5.1 Synthesis of Work

The goals of the present work are to develop methods for static aeroelastic analysis of aircraft in the preliminary design phase. An emphasis was put on the use of segregated solvers for the aerodynamic and structural models, to allow easier development and use of the tools, as well as low computational time considering the high number of computations required in the early design stages.

A static aeroelastic analysis framework is presented that consists of a nonlinear vortex lattice method, a finite element analysis solver, a geometry interpreting module, and an overarching coupling algorithm.

First, the theory behind the beam elements used to represent the structural components of the aircraft wing is shown, as well as the assembly of the solid mechanics problem and its resolution with the linear and nonlinear algorithms. The development of this structural solver is based on the work by Grozdanov [41]. Then, the vortex lattice method used to compute the aerodynamic loads on the wing is presented. It consists of a linear VLM and a nonlinear version with correction applied based on the works of Parenteau *et al.* [7] as well as the 2.5D RANS data, developed by Bourgault-Côté *et al.* [84].

Furthermore, the static aeroelastic coupling strategy that puts together the aerodynamic and the structural model is presented with attention put on the conservative interpolation of the loads on the structure using the element's shape functions. Extraction of the information about the geometry such as the planform position used to represent the wing in the VLM and the cross section of the structure used by the structural solver is automated by a CAD integration tool interfacing with Engineering Sketch Pad.

Verification as well as validation cases were also presented and discussed. Mainly, the finite element analysis method is demonstrated to perform well in predicting the deformation of beams against the theory, both in linear and nonlinear cases. Then, the order of accuracy is verified on a case of large deflections, where it is seen that the residual converges quadratically, consistent with the Newton-Raphson algorithm. Next, the performance of the aeroelastic coupling is tested with an application on HALE aircrafts that experience large deformations but for which the aerodynamic complexity is quite low. This allowed to check the accuracy of the results as well as the characteristics of the problem in terms of mesh refinement. It was also determined that both the linear and nonlinear VLM coupling gave close results and

the influence of viscous coefficient was discussed.

Next, the viscous coupling and the impacts on aeroelasticity are tested for the more challenging case of aileron reversal in transonic and supersonic flow conditions. This allowed to determine the extent to which this framework is suitable for transonic aerodynamic phenomena. Finally, the applicability of the methods developed is assessed in the case of a transonic commercial aircraft such as the CRM, where results compared to wind tunnel and other high fidelity analysis tools showed that the framework is both accurate and significantly less computationally expensive than other static aeroelastic method commonly used.

5.2 Limitations of the Proposed Solution

A first limitation of the methods developed in this work is that the aerodynamic contributions of the parts of the aircraft other than the wings are neglected. The most significant simplifications are the effects of the fuselage and the engines on the loading of the structure. Although it can be argued that the stiffness of the wing is such that loads close to the root as well as in-plane forces affect the final configuration of the wing in a lesser fashion than out-of-plane forces such as the lift, corrections could be enforced in the present framework to take these into account.

Secondly, the Euler-Bernoulli beam assumptions are an important simplification when it comes to the complex structure of an aircraft wing. Although it seems reasonable to state that the section of the wing remains perpendicular to its axis, this hypothesis could be further tested.

Lastly, it is assumed, when constructing the 2.5D RANS sectional database, that the airfoil shape is not deformed under the aerodynamic loading. Usually, the structural stiffness of this component is high, but it is important to stress that small changes in the shape of the wing's sections would greatly affect the loading, especially in transonic flight regimes.

5.3 Future Work

First of all, introducing the effects of fuselage, engines, and tail into the VLM could allow the current framework to be used more extensively for problems of flight dynamics of flexible aircrafts, even leading eventually to works on the control and aeroservoelasticity. Another important development would be the use of a panel method instead of the VLM, rendering the consideration of these components much simpler and increasing the fidelity of the analysis.

On the other hand, extending the current finite element methods for a wider range of finite

element shapes, such as triangles, quad-rectangles, and even prisms would be fairly straightforward by using the shape function formulations. This could help analyze more complex geometries, such as very flat rectangular wings.

Finally, the structural deformation problem could be cast in frequency domain by solving the unsteady eigenvalue problem. This would allow the determination of such phenomena as flutter, which are also very important in the design and certification process. The issue resides mainly in having a frequency domain formulation of the nonlinear VLM, but developments in this direction have already been made at Polytechnique [90].

REFERENCES

[1] P. Piperni, A. DeBlois, and R. Henderson, "Development of a Multilevel Multidisciplinary-Optimization Capability for an Industrial Environment," *AIAA Journal*, vol. 51, no. 10, pp. 2335–2352, Oct. 2013. [Online]. Available: http://arc.aiaa.org/doi/10.2514/1.J052180

[2] A. Rizzi, "Modeling and simulating aircraft stability and control—The SimSAC project," *Progress in Aerospace Sciences*, vol. 47, no. 8, pp. 573–588, Nov. 2011. [Online]. Available: https://linkinghub.elsevier.com/retrieve/pii/S0376042111000704

[3] E. H. Dowell and H. C. J. Curtiss, *A modern course in aeroelasticity.* Springer, 1989.

[4] T. E. Noll, J. M. Brown, M. E. Perez-Davis, S. D. Ishmael, G. C. Tiffany, and M. Gaier, "Investigation of the Helios Prototype Aircraft Mishap," p. 100.

[5] J. Katz and A. Plotkin, *Low-speed aerodynamics*, 2nd ed., ser. Cambridge aerospace series. Cambridge: Cambridge Univ. Press, 2001, no. 13, oCLC: 247847334.

[6] S. Gallay, S. Ghasemi, and E. Laurendeau, "Sweep effects on non-linear Lifting Line Theory near Stall," in *52nd Aerospace Sciences Meeting*, ser. AIAA SciTech Forum. American Institute of Aeronautics and Astronautics, Jan. 2014. [Online]. Available: https://doi.org/10.2514/6.2014-1105

[7] M. Parenteau, K. Sermeus, and E. Laurendeau, "VLM Coupled with 2.5d RANS Sectional Data for High-Lift Design." American Institute of Aeronautics and Astronautics, Jan. 2018. [Online]. Available: https://arc.aiaa.org/doi/10.2514/6.2018-1049

[8] S. I. Weiss and A. R. Amir, "Aerospace industry," Jan 2019. [Online]. Available: https://www.britannica.com/technology/aerospace-industry

[9] E. F. Crawley, H. C. Curtiss, D. A. Peters, R. H. Scanlan, and F. Sisto, *A Modern Course in Aeroelasticity*, ser. Solid Mechanics and its Applications, E. H. Dowell and G. M. L. Gladwell, Eds. Dordrecht: Springer Netherlands, 1995, vol. 32, dOI: 10.1007/978-94-011-0499-9. [Online]. Available: http://link.springer.com/10.1007/978-94-011-0499-9

[10] P. R. Spalart and V. Venkatakrishnan, "On the role and challenges of CFD in the aerospace industry," *The Aeronautical Journal*, vol. 120, no. 1223, pp. 209–232,

Jan. 2016. [Online]. Available: https://www.cambridge.org/core/product/identifier/S000192401500010X/type/journal_article

[11] T. Theodorsen, "General Theory of Aerodynamic Instability and the Mechanism of Flutter," 1935.

[12] E. d. Langre, *Fluides et solides*. Palaiseau: Editions de l'Ecole polytechnique, 2002, oCLC: 61740059.

[13] J. W. Edwards, H. Ashley, and J. V. Breakwell, "Unsteady aerodynamic modeling for arbitrary motions," *AIAA Journal*, vol. 17, no. 4, pp. 365–374, Apr. 1979. [Online]. Available: http://arc.aiaa.org/doi/10.2514/3.7348

[14] P. Marzocca, L. Librescu, D.-H. Kim, I. Lee, and S. Schober, "Development of an indicial function approach for the two-dimensional incompressible/compressible aerodynamic load modelling," *Proceedings of the Institution of Mechanical Engineers, Part G: Journal of Aerospace Engineering*, vol. 221, no. 3, pp. 453–463, Mar. 2007. [Online]. Available: http://journals.sagepub.com/doi/10.1243/09544100JAERO88

[15] S. Yang, S. Luo, F. Liu, and H.-M. Tsai, "Subsonic Flow over Unstalled Pitching Airfoil Computed by Euler Method," in *36th AIAA Fluid Dynamics Conference and Exhibit*. San Francisco, California: American Institute of Aeronautics and Astronautics, Jun. 2006. [Online]. Available: http://arc.aiaa.org/doi/10.2514/6.2006-3914

[16] M. Conner, D. Tang, E. Dowell, and L. Virgin, "NONLINEAR BEHAVIOR OF A TYPICAL AIRFOIL SECTION WITH CONTROL SURFACE FREEPLAY: A NUMERICAL AND EXPERIMENTAL STUDY," *Journal of Fluids and Structures*, vol. 11, no. 1, pp. 89–109, Jan. 1997. [Online]. Available: http://linkinghub.elsevier.com/retrieve/pii/S0889974696900687

[17] A. Abdelkefi, R. Vasconcellos, F. Marques, and M. Hajj, "Modeling and identification of freeplay nonlinearity," *Journal of Sound and Vibration*, vol. 331, no. 8, pp. 1898–1907, Apr. 2012. [Online]. Available: http://linkinghub.elsevier.com/retrieve/pii/S0022460X11009680

[18] D. B. Kholodar, "Nature of Freeplay-Induced Aeroelastic Oscillations," *Journal of Aircraft*, vol. 51, no. 2, pp. 571–583, Mar. 2014. [Online]. Available: http://arc.aiaa.org/doi/10.2514/1.C032295

[19] D. Tang, E. Dowell, and L. Virgin, "LIMIT CYCLE BEHAVIOR OF AN AIRFOIL WITH A CONTROL SURFACE," *Journal of Fluids and Structures*, vol. 12, no. 7,

pp. 839–858, Oct. 1998. [Online]. Available: http://linkinghub.elsevier.com/retrieve/pii/S0889974698901748

[20] S. T. Trickey, L. N. Virgin, and E. H. Dowell, "The stability of limit-cycle oscillations in a nonlinear aeroelastic system," *Proceedings of the Royal Society A: Mathematical, Physical and Engineering Sciences*, vol. 458, no. 2025, pp. 2203–2226, Sep. 2002. [Online]. Available: http://rspa.royalsocietypublishing.org/cgi/doi/10.1098/rspa.2002.0965

[21] Y. Zhao and H. Hu, "Aeroelastic analysis of a non-linear airfoil based on unsteady vortex lattice model," *Journal of Sound and Vibration*, vol. 276, no. 3-5, pp. 491–510, Sep. 2004. [Online]. Available: http://linkinghub.elsevier.com/retrieve/pii/S0022460X03008678

[22] D. Moxon, "Flexible Mass-Balance Arms and Control-Surface Flutter," HM Stationery Office, Tech. Rep., 1960. [Online]. Available: https://pdfs.semanticscholar.org/20a0/f692d4bd278d9d1934b867f66cb775d8c311.pdf

[23] J. D. Anderson, *Fundamentals of aerodynamics*, 5th ed., ser. Anderson series. New York: McGraw-Hill, 2011, oCLC: ocn463634144.

[24] P. Spalart and S. Allmaras, "A one-equation turbulence model for aerodynamic flows," in *30th Aerospace Sciences Meeting and Exhibit*. Reno,NV,U.S.A.: American Institute of Aeronautics and Astronautics, Jan. 1992. [Online]. Available: http://arc.aiaa.org/doi/10.2514/6.1992-439

[25] T. Cebeci, Ed., *Computational fluid dynamics for engineers: from panel to Navier-Stokes methods with computer programs*. Long Beach, Calif. : Berlin: Horizons Pub. Inc., ; Springer, 2005, oCLC: ocm60802091.

[26] R. Thormann and D. Dimitrov, "Correction of aerodynamic influence matrices for transonic flow," *CEAS Aeronautical Journal*, vol. 5, no. 4, pp. 435–446, Dec. 2014. [Online]. Available: http://link.springer.com/10.1007/s13272-014-0114-3

[27] C. van Dam, "The aerodynamic design of multi-element high-lift systems for transport airplanes," *Progress in Aerospace Sciences*, vol. 38, no. 2, pp. 101–144, Feb. 2002. [Online]. Available: http://linkinghub.elsevier.com/retrieve/pii/S0376042102000027

[28] S. Gallay and E. Laurendeau, "Nonlinear Generalized Lifting-Line Coupling Algorithms for Pre/Poststall Flows," *AIAA Journal*, vol. 53, no. 7, pp. 1784–1792, Jul. 2015. [Online]. Available: http://arc.aiaa.org/doi/10.2514/1.J053530

[29] R. D. Cook and R. D. Cook, Eds., *Concepts and applications of finite element analysis*, 4th ed. New York, NY: Wiley, 2001.

[30] O. C. Zienkiewicz, R. L. Taylor, and J. Z. Zhu, *The finite element method: its basis and fundamentals*, 7th ed. Amsterdam: Elsevier, Butterworth-Heinemann, 2013, oCLC: ocn852808496.

[31] M. S. A. Elsayed, R. Sedaghati, and M. Abdo, "Accurate Stick Model Development for Static Analysis of Complex Aircraft Wing-Box Structures," *AIAA Journal*, vol. 47, no. 9, pp. 2063–2075, Sep. 2009. [Online]. Available: http://arc.aiaa.org/doi/10.2514/1.38447

[32] H. Bdeiwi, A. Ciarella, A. Peace, and M. Hahn, "Model structure effect on static aeroelastic deformation of the NASA CRM," *International Journal of Numerical Methods for Heat & Fluid Flow*, Jan. 2019. [Online]. Available: https://www.emeraldinsight.com/doi/10.1108/HFF-07-2018-0352

[33] F. Auricchio, P. Carotenuto, and A. Reali, "On the geometrically exact beam model: A consistent, effective and simple derivation from three-dimensional finite-elasticity," *International Journal of Solids and Structures*, vol. 45, no. 17, pp. 4766–4781, Aug. 2008. [Online]. Available: http://linkinghub.elsevier.com/retrieve/pii/S0020768308001790

[34] K. M. Hsiao, "Corotational total Lagrangian formulation for three-dimensional beamelement," *AIAA Journal*, vol. 30, no. 3, pp. 797–804, Mar. 1992. [Online]. Available: http://arc.aiaa.org/doi/10.2514/3.10987

[35] K. M. Hsiao, J. Y. Lin, and W. Y. Lin, "A consistent co-rotational finite element formulation for geometrically nonlinear dynamic analysis of 3-D beams," *Computer Methods in Applied Mechanics and Engineering*, vol. 169, no. 1-2, pp. 1–18, Jan. 1999. [Online]. Available: http://linkinghub.elsevier.com/retrieve/pii/S0045782598001522

[36] A. Banerjee, B. Bhattacharya, and A. Mallik, "Large deflection of cantilever beams with geometric non-linearity: Analytical and numerical approaches," *International Journal of Non-Linear Mechanics*, vol. 43, no. 5, pp. 366–376, Jun. 2008. [Online]. Available: http://linkinghub.elsevier.com/retrieve/pii/S0020746208000048

[37] C. Farhat and M. Lesoinne, "Two efficient staggered algorithms for the serial and parallel solution of three-dimensional nonlinear transient aeroelastic problems," *Computer Methods in Applied Mechanics and Engineering*, vol. 182, no. 3-4, pp. 499–515, Feb. 2000. [Online]. Available: http://linkinghub.elsevier.com/retrieve/pii/S0045782599002066

[38] S. Piperno, C. Farhat, and B. Larrouturou, "Partitioned procedures for the transient solution of coupled aroelastic problems Part I: Model problem, theory and two-dimensional application," *Computer Methods in Applied Mechanics and Engineering*, vol. 124, no. 1-2, pp. 79–112, Jun. 1995. [Online]. Available: https://linkinghub.elsevier.com/retrieve/pii/0045782595927079

[39] C. Farhat, M. Lesoinne, and P. Le Tallec, "Load and motion transfer algorithms for fluid/structure interaction problems with non-matching discrete interfaces: Momentum and energy conservation, optimal discretization and application to aeroelasticity," *Computer Methods in Applied Mechanics and Engineering*, vol. 157, no. 1-2, pp. 95–114, Apr. 1998. [Online]. Available: http://linkinghub.elsevier.com/retrieve/pii/S0045782597002168

[40] A. Beckert and H. Wendland, "Multivariate interpolation for fluid-structure-interaction problems using radial basis functions," *Aerospace Science and Technology*, vol. 5, no. 2, pp. 125–134, Feb. 2001. [Online]. Available: http://linkinghub.elsevier.com/retrieve/pii/S1270963800010877

[41] A. Grozdanov and E. Laurendeau, "Assessment of Numerical Tools to Predict Control Surface Effectiveness." International Forum on Aeroelasticity and Structural Dynamics, Jun. 2017.

[42] M. Smith, M. Patil, and D. Hodges, "CFD-based analysis of nonlinear aeroelastic behavior of high-aspect ratio wings." American Institute of Aeronautics and Astronautics, Jun. 2001. [Online]. Available: http://arc.aiaa.org/doi/10.2514/6.2001-1582

[43] J. Murua, R. Palacios, and J. M. R. Graham, "Applications of the unsteady vortex-lattice method in aircraft aeroelasticity and flight dynamics," *Progress in Aerospace Sciences*, vol. 55, pp. 46–72, Nov. 2012. [Online]. Available: http://linkinghub.elsevier.com/retrieve/pii/S0376042112000620

[44] F. Afonso, J. Vale, E. Oliveira, F. Lau, and A. Suleman, "A review on non-linear aeroelasticity of high aspect-ratio wings," *Progress in Aerospace Sciences*, vol. 89, pp. 40–57, Feb. 2017. [Online]. Available: http://linkinghub.elsevier.com/retrieve/pii/S037604211630077X

[45] S. Keye, "Fluid-Structure Coupled Analysis of a Transport Aircraft and Flight-Test Validation," *Journal of Aircraft*, vol. 48, no. 2, pp. 381–390, Mar. 2011. [Online]. Available: http://arc.aiaa.org/doi/10.2514/1.C000235

[46] S. Keye, V. Togiti, B. Eisfeld, O. Brodersen, and M. B. Rivers, "Investigation of Fluid-Structure-Coupling and Turbulence Model Effects on the DLR Results of the Fifth AIAA CFD Drag Prediction Workshop," *AIAA Paper*, vol. 2509, p. 2013, 2013. [Online]. Available: https://arc.aiaa.org/doi/pdfplus/10.2514/6.2013-2509

[47] J.-L. Hantrais-Gervois, A. Lepage, F. Ternoy, G. Carraz, and G. Jeanfaivre, "Transonic Aeroelasticity using the 2.5d Non-Linear Vortex-Lattice Method." American Institute of Aeronautics and Astronautics, Jun. 2010. [Online]. Available: http://arc.aiaa.org/doi/10.2514/6.2010-4816

[48] P. Chwalowski, J. P. Florance, J. Heeg, C. D. Wieseman, and B. P. Perry, "Preliminary computational analysis of the (hirenasd) configuration in preparation for the aeroelastic prediction workshop," Jun. 2011. [Online]. Available: https://ntrs.nasa.gov/search.jsp?R=20110015415

[49] A. Arena, W. Lacarbonara, and P. Marzocca, "Nonlinear Aeroelastic Formulation and Postflutter Analysis of Flexible High-Aspect-Ratio Wings," *Journal of Aircraft*, vol. 50, no. 6, pp. 1748–1764, Nov. 2013. [Online]. Available: http://arc.aiaa.org/doi/10.2514/1.C032145

[50] C. de Souza, R. G. da Silva, and C. Cesnik, "Nonlinear Aeroelastic Framework Based on Vortex-Lattice Method and Corotational Shell Finite Element." American Institute of Aeronautics and Astronautics, Apr. 2012. [Online]. Available: http://arc.aiaa.org/doi/abs/10.2514/6.2012-1976

[51] J. Murua, "'Flexible aircraft dynamics with a geometrically-nonlinear description of the unsteady aerodynamics'," Ph.D. dissertation, Imperial College London, 2012. [Online]. Available: http://epubs.surrey.ac.uk/726466/

[52] N. T. Nguyen, E. Ting, and D. Chaparro, "Nonlinear Large Deflection Theory with Modified Aeroelastic Lifting Line Aerodynamics for a High Aspect Ratio Flexible Wing." American Institute of Aeronautics and Astronautics, Jun. 2017. [Online]. Available: https://arc.aiaa.org/doi/10.2514/6.2017-4219

[53] M. Patil, D. Hodges, and C. Cesnik, "Nonlinear aeroelastic analysis of aircraft with high-aspect-ratio wings." American Institute of Aeronautics and Astronautics, Apr. 1998. [Online]. Available: http://arc.aiaa.org/doi/10.2514/6.1998-1955

[54] C. Spada, "Aeroelastic Analysis of Nonlinear High Aspect Ratio Wings," 2014. [Online]. Available: https://fenix.tecnico.ulisboa.pt/downloadFile/844820067123515/Final%20version_V0.pdf

[55] C. Spada, F. Afonso, F. Lau, and A. Suleman, "Nonlinear aeroelastic scaling of high aspect-ratio wings," *Aerospace Science and Technology*, vol. 63, pp. 363–371, Apr. 2017. [Online]. Available: http://linkinghub.elsevier.com/retrieve/pii/S1270963817301074

[56] R. J. Simpson and R. Palacios, "Numerical aspects of nonlinear flexible aircraft flight dynamics modeling." American Institute of Aeronautics and Astronautics, Apr. 2013. [Online]. Available: http://arc.aiaa.org/doi/10.2514/6.2013-1634

[57] R. J. Simpson, R. Palacios, and S. Maraniello, "State-space realizations of potential-flow unsteady aerodynamics with arbitrary kinematics." American Institute of Aeronautics and Astronautics, Jan. 2017. [Online]. Available: http://arc.aiaa.org/doi/10.2514/6.2017-1595

[58] R. Palacios, J. Murua, and R. Cook, "Structural and Aerodynamic Models in Nonlinear Flight Dynamics of Very Flexible Aircraft," *AIAA Journal*, vol. 48, no. 11, pp. 2648–2659, Nov. 2010. [Online]. Available: http://arc.aiaa.org/doi/10.2514/1.J050513

[59] R. C. Paul, J. Murua, and A. Gopalarathnam, "Unsteady and Post-Stall Aerodynamic Modeling for Flight Dynamics Simulation." American Institute of Aeronautics and Astronautics, Jan. 2014. [Online]. Available: http://arc.aiaa.org/doi/10.2514/6.2014-0729

[60] R. J. S. Simpson, R. Palacios, and J. Murua, "Induced-Drag Calculations in the Unsteady Vortex Lattice Method," *AIAA Journal*, vol. 51, no. 7, pp. 1775–1779, Jul. 2013. [Online]. Available: http://arc.aiaa.org/doi/10.2514/1.J052136

[61] G. P. Guruswamy and P. M. Goorjian, "Unsteady transonic aerodynamics and aeroelastic calculations at low-supersonic freestreams," *Journal of aircraft*, vol. 25, no. 10, pp. 955–961, 1988. [Online]. Available: https://arc.aiaa.org/doi/pdfplus/10.2514/3.45685

[62] P. Mantegazza and S. Ricci, "Direct approach to the analysis of control reversal and its sensitivity," *AIAA Journal*, vol. 28, no. 11, pp. 1995–1996, Nov. 1990. [Online]. Available: http://arc.aiaa.org/doi/10.2514/3.10510

[63] G. Andersen, R. Kolonay, and F. Eastep, "Control-Surface Reversal in the Transonic Regime," *Journal of Aircraft*, vol. 35, no. 5, pp. 688–694, Sep. 1998. [Online]. Available: http://arc.aiaa.org/doi/10.2514/2.2378

[64] F. Eastep, G. Andersen, P. Beran, and R. Kolonay, "Control Surface Reversal in the Transonic Regime Including Viscous Effects," *Journal of Aircraft*, vol. 38, no. 4, pp. 653–663, Jul. 2001. [Online]. Available: http://arc.aiaa.org/doi/10.2514/2.2842

[65] F. Eastep, E. Thompson, R. Kolonay, J. Camberos, and R. Grandhi, "Investigating the Effect of Structural Design on Control Surface Reversal Using Velocity Transpiration Enabled Euler Flow Solver." American Institute of Aeronautics and Astronautics, Jan. 2009. [Online]. Available: http://arc.aiaa.org/doi/10.2514/6.2009-1462

[66] K.-T. Kim and O. Song, "Aileron Reversal of Nonuniform and Swept Composite Aircraft Wings," *Journal of Aircraft*, vol. 50, no. 3, pp. 681–693, May 2013. [Online]. Available: http://arc.aiaa.org/doi/10.2514/1.C031212

[67] N. Yoon, C. Chung, Y.-H. Na, and S. Shin, "Control reversal and torsional divergence analysis for a high-aspect-ratio wing," *Journal of Mechanical Science and Technology*, vol. 26, no. 12, pp. 3921–3931, Dec. 2012. [Online]. Available: http://link.springer.com/10.1007/s12206-012-0889-2

[68] T. Mauermann, "Flexible Aircraft Modelling for Flight Loads Analysis of Wake Vortex Encounters," Ph.D. dissertation, DLR, 2011. [Online]. Available: http://www.exercicescorriges.com/i_203868.pdf

[69] S. Keye and R. Rudnik, "Aero-elastic simulation of DLR's F6 transport aircraft configuration and comparison to experimental data," *AIAA Paper*, vol. 580, p. 2009, 2009. [Online]. Available: https://arc.aiaa.org/doi/pdfplus/10.2514/6.2009-580

[70] S. Keye, O. Brodersen, and M. B. Rivers, "Investigation of Aeroelastic Effects on the NASA Common Research Model," *Journal of Aircraft*, vol. 51, no. 4, pp. 1323–1330, Jul. 2014. [Online]. Available: http://arc.aiaa.org/doi/10.2514/1.C032598

[71] S. Hernández, E. Menga, P. Naveira, D. Freire, C. López, M. Cid Montoya, S. Moledo, and A. Baldomir, "Dynamic analysis of assembled aircraft structures considering interfaces with nonlinear behavior," *Aerospace Science and Technology*, vol. 77, pp. 265–272, Jun. 2018. [Online]. Available: http://linkinghub.elsevier.com/retrieve/pii/S1270963817313962

[72] L. Cavagna, S. Ricci, and L. Riccobene, "Structural Sizing, Aeroelastic Analysis, and Optimization in Aircraft Conceptual Design," *Journal of Aircraft*, vol. 48, no. 6, pp. 1840–1855, Nov. 2011. [Online]. Available: http://arc.aiaa.org/doi/10.2514/1.C031072

[73] A. DeBlois and M. Abdo, "Multi-fidelity multidisciplinary design optimization of metallic and composite regional and business jets," *AIAA Paper*, vol. 9191, p. 25, 2010. [Online]. Available: https://arc.aiaa.org/doi/pdf/10.2514/6.2010-9191

[74] A. Elham and M. J. L. van Tooren, "Coupled adjoint aerostructural wing optimization using quasi-three-dimensional aerodynamic analysis," *Structural and Multidisciplinary Optimization*, vol. 54, pp. 889–906, May 2016. [Online]. Available: http://link.springer.com/10.1007/s00158-016-1447-9

[75] R. Kolonay, M. Dindar, M. Love, and A. De La Garza, "A methodology of large scale computational aeroelasticity for the MDA/MDO environment." American Institute of Aeronautics and Astronautics, Sep. 2000. [Online]. Available: http://arc.aiaa.org/doi/10.2514/6.2000-4789

[76] F. Mastroddi and S. Gemma, "Analysis of Pareto frontiers for multidisciplinary design optimization of aircraft," *Aerospace Science and Technology*, vol. 28, no. 1, pp. 40–55, Jul. 2013. [Online]. Available: http://linkinghub.elsevier.com/retrieve/pii/S1270963812001538

[77] P. Piperni, M. Abdo, F. Kafyeke, and A. T. Isikveren, "Preliminary Aerostructural Optimization of a Large Business Jet," *Journal of Aircraft*, vol. 44, no. 5, pp. 1422–1438, Sep. 2007. [Online]. Available: http://arc.aiaa.org/doi/10.2514/1.26989

[78] M. Parenteau, E. Laurendeau, and G. Carrier, "Combined high-speed and high-lift wing aerodynamic optimization using a coupled VLM-2.5d RANS approach," *Aerospace Science and Technology*, vol. 76, pp. 484–496, May 2018. [Online]. Available: http://linkinghub.elsevier.com/retrieve/pii/S1270963817317790

[79] A. Pigeon, A. T. Levesque, and E. Laurendeau, "Two-dimensional navier–stokes flow solver developments at ecole polytechnique de montreal." CFD Society of Canada 22nd Annual Conference, CFD Society of Canada, Jun. 2014.

[80] J. Blazek, *Computational Fluid Dynamics: Principles and Applications*, ser. Computational Fluid Dynamics: Principles and Applications. Elsevier Science, 2001, no. vol. 1. [Online]. Available: https://books.google.fr/books?id=yPVQAAAAMAAJ

[81] A. Jameson, W. Schmidt, and E. Turkel, "Numerical solutions of the euler equations by finite volume methods using runge-kutta time-stepping schemes." AIAA paper 1981-1259, Jun. 1981.

[82] R. Swanson, R. Radespiel, and E. Turkel, "On some numerical dissipation schemes," *Journal of Computational Physics*, vol. 147, no. 2, pp. 518 – 544, 1998. [Online]. Available: http://www.sciencedirect.com/science/article/pii/S0021999198961009

[83] A. Jameson, "Multigrid algorithms for compressible flow calculations," in *Multigrid Methods II*, W. Hackbusch and U. Trottenberg, Eds. Berlin, Heidelberg: Springer Berlin Heidelberg, 1986, pp. 166–201.

[84] S. Bourgault-Cote, S. Ghasemi, A. Mosahebi, and E. Laurendeau, "Extension of a Two-Dimensional Navier–Stokes Solver for Infinite Swept Flow," *AIAA Journal*, vol. 55, no. 2, pp. 662–667, Feb. 2017. [Online]. Available: http://arc.aiaa.org/doi/10.2514/1.J055139

[85] R. Mukherjee and A. Gopalarathnam, "Post-stall prediction of multiple-lifting-surface configurations using a decambering approach," *Journal of Aircraft - J AIRCRAFT*, vol. 43, pp. 660–668, 05 2006.

[86] A. Kontogiannis, M. Parenteau, and E. Laurendeau, "Viscous-Inviscid Analysis of Transonic Swept Wings using 2.5d RANS and Parametric Shapes," in *AIAA Scitech 2019 Forum*. San Diego, California: American Institute of Aeronautics and Astronautics, Jan. 2019. [Online]. Available: https://arc.aiaa.org/doi/10.2514/6.2019-2116

[87] M. H. Singer, "A general approach to moment calculation for polygons and line segments," *Pattern Recognition*, vol. 26, no. 7, pp. 1019–1028, 1993. [Online]. Available: http://www.sciencedirect.com/science/article/pii/003132039390003F

[88] N. Nastran, "Handbook of Nonlinear Analysis (Solutions 106 and 129)," Tech. Rep.

[89] J. Vassberg, M. Dehaan, M. Rivers, and R. Wahls, "Development of a Common Research Model for Applied CFD Validation Studies." Honolulu, Hawaii: American Institute of Aeronautics and Astronautics, Aug. 2008. [Online]. Available: http://arc.aiaa.org/doi/10.2514/6.2008-6919

[90] M. Parenteau and E. Laurendeau, "Time Spectral Method Applied to the Unsteady Vortex Lattice Method Coupled with Viscous Sectional Data," Glasgow, UK, Jun. 2018, p. 1.

APPENDIX A MATRIX FORMULATION OF THEODORSEN EQUATIONS OF MOTION

This section details the development of the equations of motion for the 2 dof and 3 dof airfoil. The parameters and conventions used are first described before the equations are presented. The system is illustrated in figures A.1 and A.2.

first of all, the three degrees of freedom in question are heaving (h), pitching (α), and aileron deflection (β). In the case of a 2 degrees of freedom system, the aileron is non existent and the deflection is therefore always 0.

The stiffness associated with each degree of freedom is noted respectively K_h, K_α, and K_β.

The mass and inertia terms are as follows :

- I_α = moment of inertia of the entire airfoil about a
- S_α = static moment of the entire airfoil about a
- I_β = moment of inertia of the entire airfoil about c
- S_β = static moment of the entire airfoil about c
- x_α = center of gravity of the entire airfoil
- x_β = center of gravity of the aileron

Where a is shown in the figures to be the point of rotation. This distance is taken from the center of the section to the elastic axis. Accordingly, c is the position of the hinge of the aileron taken from the center of the section. It is also important to stress that the half-chord is the reference lengthm designated as b,

From (Theodorsen, 1935), the equations of motion for the 3dof airfoil are as follows :

$$M\ddot{h} + S_\alpha\ddot{\alpha} + S_\beta\ddot{\beta} + K_h h = L \tag{A.1}$$

$$S_\alpha\ddot{h} + I_\alpha\ddot{\alpha} + I_\beta\ddot{\beta} + b(c-a)S_\beta\ddot{\beta} + K_\alpha\alpha = M_\alpha \tag{A.2}$$

$$S_\beta\ddot{h} + I_\beta\ddot{\alpha} + b(c-a)S_\beta\ddot{\alpha} + I_\beta\ddot{\beta} + b(c-a)S_\beta\ddot{\beta} + K_\beta\beta = M_\beta \tag{A.3}$$

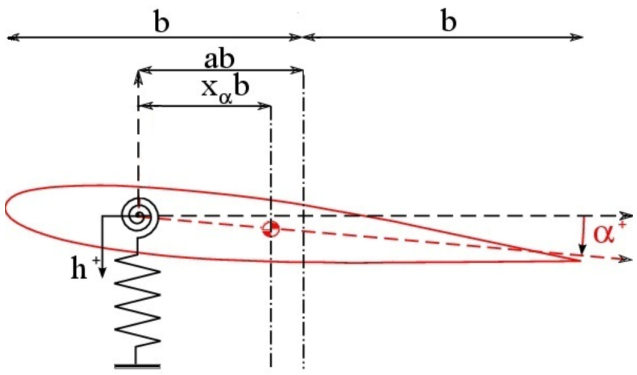

Figure A.1 2 degrees-of-freedom airfoil notation

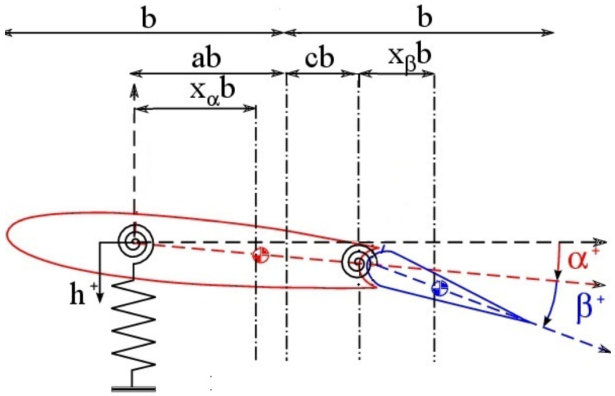

Figure A.2 3 degrees-of-freedom airfoil notation

Which can also be expressed as :

$$\begin{bmatrix} M & S_\alpha & S_\beta \\ S_\alpha & I_\alpha & I_\beta + b(c-a)S_\beta \\ S_\beta & I_\beta + b(c-a)S_\beta & I_\beta \end{bmatrix} \begin{pmatrix} \ddot{h} \\ \ddot{\alpha} \\ \ddot{\beta} \end{pmatrix} + \begin{bmatrix} M{\omega_h}^2 & 0 & 0 \\ 0 & I_\alpha {\omega_\alpha}^2 & 0 \\ 0 & 0 & I_\beta {\omega_\beta}^2 \end{bmatrix} \begin{pmatrix} h \\ \alpha \\ \beta \end{pmatrix} = \begin{pmatrix} L \\ M_\alpha \\ M_\beta \end{pmatrix} \tag{A.4}$$

It is more convenient to non dimensionnalize h to not have to bother with units. The common factor is $1/b$, the half-chord. Therefore :

$$\begin{pmatrix} h \\ \alpha \\ \beta \end{pmatrix} = \begin{bmatrix} b & 0 & 0 \\ 0 & 1 & 0 \\ 0 & 0 & 1 \end{bmatrix} \begin{pmatrix} h/b \\ \alpha \\ \beta \end{pmatrix} \tag{A.5}$$

and the following notation is adopted $h/b = \bar{h}$. By substituting equation A.5 in A.4

$$\begin{bmatrix} Mb & S_\alpha & S_\beta \\ S_\alpha b & I_\alpha & I_\beta + b(c-a)S_\beta \\ S_\beta b & I_\beta + b(c-a)S_\beta & I_\beta \end{bmatrix} \begin{pmatrix} \ddot{\bar{h}} \\ \ddot{\alpha} \\ \ddot{\beta} \end{pmatrix} + \begin{bmatrix} Mb{\omega_h}^2 & 0 & 0 \\ 0 & I_\alpha {\omega_\alpha}^2 & 0 \\ 0 & 0 & I_\beta {\omega_\beta}^2 \end{bmatrix} \begin{pmatrix} \bar{h} \\ \alpha \\ \beta \end{pmatrix} = \begin{pmatrix} L \\ M_\alpha \\ M_\beta \end{pmatrix} \tag{A.6}$$

A useful simplification can be exposed by dividing both sides of the equation by Mb^2 and distributing

$$\begin{bmatrix} Mb/Mb^2 & S_\alpha/Mb^2 & S_\beta/Mb^2 \\ S_\alpha b/Mb^2 & I_\alpha/Mb^2 & I_\beta/Mb^2 + b(c-a)S_\beta/Mb^2 \\ S_\beta b/Mb^2 & I_\beta/Mb^2 + b(c-a)S_\beta/Mb^2 & I_\beta/Mb^2 \end{bmatrix} \begin{pmatrix} \ddot{\bar{h}} \\ \ddot{\alpha} \\ \ddot{\beta} \end{pmatrix} + \begin{bmatrix} Mb{\omega_h}^2/Mb^2 & 0 & 0 \\ 0 & I_\alpha {\omega_\alpha}^2/Mb^2 & 0 \\ 0 & 0 & I_\beta {\omega_\beta}^2/Mb^2 \end{bmatrix} \begin{pmatrix} \bar{h} \\ \alpha \\ \beta \end{pmatrix} = \begin{pmatrix} L/Mb^2 \\ M_\alpha/Mb^2 \\ M_\beta/Mb^2 \end{pmatrix} \tag{A.7}$$

Equation A.7 can be simplified by knowing the following definitions :

$$x_\alpha = \frac{S_\alpha}{Mb}, x_\beta = \frac{S_\beta}{Mb}, {r_\alpha}^2 = \frac{I_\alpha}{Mb^2}, {r_\beta}^2 = \frac{I_\beta}{Mb^2}$$

giving

$$\begin{bmatrix} 1/b & x_\alpha/b & x_\beta/b \\ x_\alpha & {r_\alpha}^2 & {r_\beta}^2 + (c-a)x_\beta \\ x_\beta & {r_\beta}^2 + (c-a)x_\beta & {r_\beta}^2 \end{bmatrix} \begin{pmatrix} \ddot{\bar{h}} \\ \ddot{\alpha} \\ \ddot{\beta} \end{pmatrix} + \begin{bmatrix} {\omega_h}^2/b & 0 & 0 \\ 0 & {r_\alpha}^2{\omega_\alpha}^2 & 0 \\ 0 & 0 & {r_\beta}^2{\omega_\beta}^2 \end{bmatrix} \begin{pmatrix} \bar{h} \\ \alpha \\ \beta \end{pmatrix} = \begin{pmatrix} L/Mb^2 \\ M_\alpha/Mb^2 \\ M_\beta/Mb^2 \end{pmatrix} \tag{A.8}$$

L should be divided by $1/Mb$ instead of $1/Mb^2$, so we get

$$\begin{bmatrix} 1 & x_\alpha & x_\beta \\ x_\alpha & {r_\alpha}^2 & {r_\beta}^2 + (c-a)x_\beta \\ x_\beta & {r_\beta}^2 + (c-a)x_\beta & {r_\beta}^2 \end{bmatrix} \begin{pmatrix} \ddot{\bar{h}} \\ \ddot{\alpha} \\ \ddot{\beta} \end{pmatrix} + \begin{bmatrix} {\omega_h}^2 & 0 & 0 \\ 0 & {r_\alpha}^2{\omega_\alpha}^2 & 0 \\ 0 & 0 & {r_\beta}^2{\omega_\beta}^2 \end{bmatrix} \begin{pmatrix} \bar{h} \\ \alpha \\ \beta \end{pmatrix} = \begin{pmatrix} L/Mb \\ M_\alpha/Mb^2 \\ M_\beta/Mb^2 \end{pmatrix} \tag{A.9}$$

There is a change of variable used to nondimensionalize the time quantity $\tau = \omega_a \alpha t$ introduced with the time derivative $\frac{dh}{d\tau} = \frac{dh}{dt}\frac{dt\omega_a\alpha}{d\tau}$. Thus,

$${\omega_\alpha}^2 \begin{bmatrix} 1 & x_\alpha & x_\beta \\ x_\alpha & {r_\alpha}^2 & {r_\beta}^2 + (c-a)x_\beta \\ x_\beta & {r_\beta}^2 + (c-a)x_\beta & {r_\beta}^2 \end{bmatrix} \begin{pmatrix} \ddot{\bar{h}} \\ \ddot{\alpha} \\ \ddot{\beta} \end{pmatrix} + \begin{bmatrix} {\omega_h}^2 & 0 & 0 \\ 0 & {r_\alpha}^2{\omega_\alpha}^2 & 0 \\ 0 & 0 & {r_\beta}^2{\omega_\beta}^2 \end{bmatrix} \begin{pmatrix} \bar{h} \\ \alpha \\ \beta \end{pmatrix} = \begin{pmatrix} L/Mb \\ M_\alpha/Mb^2 \\ M_\beta/Mb^2 \end{pmatrix} \tag{A.10}$$

and by simplifying both sides by ${\omega_\alpha}^2$

$$\begin{bmatrix} 1 & x_\alpha & x_\beta \\ x_\alpha & {r_\alpha}^2 & {r_\beta}^2 + (c-a)x_\beta \\ x_\beta & {r_\beta}^2 + (c-a)x_\beta & {r_\beta}^2 \end{bmatrix} \begin{pmatrix} \ddot{\bar{h}} \\ \ddot{\alpha} \\ \ddot{\beta} \end{pmatrix} + \begin{bmatrix} {\omega_h}^2/{\omega_\alpha}^2 & 0 & 0 \\ 0 & {r_\alpha}^2 & 0 \\ 0 & 0 & {r_\beta}^2{\omega_\beta}^2/{\omega_\alpha}^2 \end{bmatrix} \begin{pmatrix} \bar{h} \\ \alpha \\ \beta \end{pmatrix} = \begin{pmatrix} L/Mb{\omega_\alpha}^2 \\ M_\alpha/Mb^2{\omega_\alpha}^2 \\ M_\beta/Mb^2{\omega_\alpha}^2 \end{pmatrix} \tag{A.11}$$

When only 2 degrees-of-freedom are considered (h & α), this equation reduces to

$$\begin{bmatrix} 1 & x_\alpha \\ x_\alpha & {r_\alpha}^2 \end{bmatrix} \begin{pmatrix} \ddot{\bar{h}} \\ \ddot{\alpha} \end{pmatrix} + \begin{bmatrix} {\omega_h}^2 & 0 \\ 0 & {r_\alpha}^2{\omega_\alpha}^2 \end{bmatrix} \begin{pmatrix} \bar{h} \\ \alpha \end{pmatrix} = \begin{pmatrix} L/Mb \\ M_\alpha/Mb^2 \end{pmatrix} \tag{A.12}$$

The addition of damping to the system is as follows

$$\begin{bmatrix} M & S_\alpha & S_\beta \\ S_\alpha & I_\alpha & I_\beta + b(c-a)S_\beta \\ S_\beta & I_\beta + b(c-a)S_\beta & I_\beta \end{bmatrix} \begin{pmatrix} \ddot{h} \\ \ddot{\alpha} \\ \ddot{\beta} \end{pmatrix} + \frac{1}{W} \begin{bmatrix} g_h M {\omega_h}^2 & 0 & 0 \\ 0 & g_\alpha I_\alpha {\omega_\alpha}^2 & 0 \\ 0 & 0 & g_\beta I_\beta {\omega_\beta}^2 \end{bmatrix} \begin{pmatrix} \dot{h} \\ \dot{\alpha} \\ \dot{\beta} \end{pmatrix} + \begin{bmatrix} M\omega_h & 0 & 0 \\ 0 & I_\alpha \omega_\alpha & 0 \\ 0 & 0 & I_\beta \omega_\beta \end{bmatrix} \begin{pmatrix} h \\ \alpha \\ \beta \end{pmatrix} = \begin{pmatrix} L \\ M_\alpha \\ M_\beta \end{pmatrix} \tag{A.13}$$

which, after the simplifications outlined above, becomes

$$\begin{bmatrix} 1 & x_\alpha & x_\beta \\ x_\alpha & {r_\alpha}^2 & {r_\beta}^2 + (c-a)x_\beta \\ x_\beta & {r_\beta}^2 + (c-a)x_\beta & {r_\beta}^2 \end{bmatrix} \begin{pmatrix} \ddot{\bar{h}} \\ \ddot{\alpha} \\ \ddot{\beta} \end{pmatrix} + \frac{1}{W} \begin{bmatrix} g_h {\omega_h}^2 & 0 & 0 \\ 0 & g_\alpha {r_\alpha}^2 {\omega_\alpha}^2 & 0 \\ 0 & 0 & g_\beta {r_\beta}^2 {\omega_\beta}^2 \end{bmatrix} \begin{pmatrix} \dot{\bar{h}} \\ \dot{\alpha} \\ \dot{\beta} \end{pmatrix} + \begin{bmatrix} {\omega_h}^2 & 0 & 0 \\ 0 & {r_\alpha}^2 {\omega_\alpha}^2 & 0 \\ 0 & 0 & {r_\beta}^2 {\omega_\beta}^2 \end{bmatrix} \begin{pmatrix} \bar{h} \\ \alpha \\ \beta \end{pmatrix} = \begin{pmatrix} L/Mb \\ M_\alpha/Mb^2 \\ M_\beta/Mb^2 \end{pmatrix} \tag{A.14}$$

APPENDIX B STRESS-STRAIN RELATIONSHIP

This appendix develops the stress-strain relationship for normal and shear stress into the more useful compliance matrix, which expresses the stresses as a function of the strains instead of the opposite. From the equations of the strains (ϵ) as a function of the normal stresses (σ):

$$\epsilon_x = (\sigma_x - \nu(\sigma y + \sigma z))/E \tag{B.1a}$$
$$\epsilon_y = (\sigma_y - \nu(\sigma x + \sigma z))/E \tag{B.1b}$$
$$\epsilon_z = (\sigma_z - \nu(\sigma x + \sigma y))/E \tag{B.1c}$$

It is possible to change the reorder each equation to obtain:

$$\sigma_x = E\epsilon_x + \nu\sigma y + \nu\sigma z \tag{B.2a}$$
$$\sigma_y = E\epsilon_y + \nu\sigma x + \nu\sigma z \tag{B.2b}$$
$$\sigma_z = E\epsilon_z + \nu\sigma x + \nu\sigma y \tag{B.2c}$$

The equations can then be subtracted to substitute and solve for σ_x. The first line is subtracted from lines 2 and 3:

$$\sigma_x = E\epsilon_x + \nu\sigma y + \nu\sigma z \tag{B.3a}$$
$$\sigma_y = \frac{E}{1+\nu}(\epsilon_y - \epsilon_x) + \sigma x \tag{B.3b}$$
$$\sigma_z = \frac{E}{1+\nu}(\epsilon_z - \epsilon_x) + \sigma x \tag{B.3c}$$

By substituting the expressions of σ_y and σ_z we get:

$$\sigma_x = E\epsilon_x + \frac{\nu E}{(1+\nu)}(\epsilon_y - \epsilon_x) + \nu\sigma x + \frac{\nu E}{(1+\nu)}(\epsilon_z - \epsilon_x) + \nu\sigma x \tag{B.4}$$

And by rearranging:

$$\sigma_x = E\epsilon_x + \frac{\nu E}{(1+\nu)}(\epsilon_y + \epsilon_z - 2\epsilon_x) + 2\nu\sigma x \tag{B.5}$$

Which gives:

$$\sigma_x = \frac{E}{(1+\nu)(1-2\nu)}((1-\nu)\epsilon_x + \nu\epsilon_y + \nu\epsilon_z) \tag{B.6}$$

And a similar process is repeated for to isolate σ_y and σ_z. For the shear stress, the relationships are much easier to isolate:

$$\gamma_{xy} = \frac{\tau_{xy}}{G} = \frac{2(1+\nu)}{E}\tau_{xy} \tag{B.7}$$

Thus

$$\tau_{xy} = \frac{E}{2(1+\nu)}\gamma_{xy} = \frac{E}{(1+\nu)(1-2\nu)} \cdot \frac{1-2\nu}{2}\gamma_{xy} = \frac{E}{(1+\nu)(1-2\nu)} \cdot (1/2-\nu)\gamma_{xy} \tag{B.8}$$

Giving the following system of linear equations:

$$\begin{pmatrix} \sigma_x \\ \sigma_y \\ \sigma_z \\ \tau_{xy} \\ \tau_{yz} \\ \tau_{xz} \end{pmatrix} = \frac{E}{(1+\nu)(1-2\nu)} \begin{bmatrix} 1-\nu & \nu & \nu & & & \\ \nu & 1-\nu & \nu & & & \\ \nu & \nu & 1-\nu & & & \\ & & & \frac{1}{2}-\nu & & \\ & & & & \frac{1}{2}-\nu & \\ & & & & & \frac{1}{2}-\nu \end{bmatrix} \begin{pmatrix} \epsilon_x \\ \epsilon_y \\ \epsilon_z \\ \gamma_{xy} \\ \gamma_{yz} \\ \gamma_{xz} \end{pmatrix} \tag{B.9}$$

And the inverse of Eq. (3.3) is indeed Eq. (3.4).